

Energy & Environmental Science

Accepted Manuscript



This is an *Accepted Manuscript*, which has been through the Royal Society of Chemistry peer review process and has been accepted for publication.

Accepted Manuscripts are published online shortly after acceptance, before technical editing, formatting and proof reading. Using this free service, authors can make their results available to the community, in citable form, before we publish the edited article. We will replace this *Accepted Manuscript* with the edited and formatted *Advance Article* as soon as it is available.

You can find more information about *Accepted Manuscripts* in the [Information for Authors](#).

Please note that technical editing may introduce minor changes to the text and/or graphics, which may alter content. The journal's standard [Terms & Conditions](#) and the [Ethical guidelines](#) still apply. In no event shall the Royal Society of Chemistry be held responsible for any errors or omissions in this *Accepted Manuscript* or any consequences arising from the use of any information it contains.

Titanium Incorporation into Hematite Photoelectrodes: Theoretical Considerations and Experimental Observations

C. X. Kronawitter^a, I. Zegkinoglou^{b,c}, S.-H. Shen^b, P. Liao^{d,e}, I. S. Cho^f, O. Zandi^g, Y.-S. Liu^c, K. Lashgari^h, G. Westin^{h,b,k}, J.-H. Guo^c, F. J. Himpselⁱ, E. A. Carter^d, X. L. Zheng^f, T. W. Hamann^g, B. E. Koel^a, S. S. Mao^{j,k,*}, L. Vayssieres^{b,*}

^aDepartment of Chemical and Biological Engineering, Princeton University, Princeton, NJ 08544 (USA)

^bInternational Research Center for Renewable Energy, State Key Laboratory of Multiphase Flow in Power Engineering, Xi'an Jiaotong University, Xi'an 710049 (P. R. China)

^cAdvanced Light Source, Lawrence Berkeley National Laboratory, Berkeley, CA 94720 (USA)

^dDepartment of Mechanical and Aerospace Engineering, Program in Applied and Computational Mathematics, and Andlinger Center for Energy and the Environment, Princeton University, Princeton, New Jersey 08544

^eDepartment of Chemistry, Columbia University, New York, NY 10027

^fDepartment of Mechanical Engineering, Stanford University, Stanford, CA, 94305 (USA)

^gDepartment of Chemistry, Michigan State University, East Lansing, MI 48824 (USA)

^hDepartment of Chemistry-Ångström, Uppsala University, Uppsala 75121 (Sweden)

ⁱDepartment of Physics, University of Wisconsin Madison, Madison, WI 53706 (USA)

^jDepartment of Mechanical Engineering, University of California at Berkeley, Berkeley, CA 94720 (USA)

^kInternational Institute of New Energy, Shenzhen 518031 (P. R. China)

Abstract

A theoretical and experimental perspective on the role of titanium impurities in hematite (α -Fe₂O₃) nanostructured photoelectrodes for solar fuel synthesis devices is provided. Titanium incorporation is a known correlate to efficiency enhancement in α -Fe₂O₃ photoanodes for solar water oxidation; here relevant literature and the latest advances are presented and various proposed mechanisms for enhancement are contrasted. Available experimental evidence suggests that Ti incorporation increases net electron carrier concentrations in electrodes, most likely to the extent that (synthesis-dependent) charge compensating cation vacancies are not present. However, electron conductivity increases alone cannot quantitatively account for the large associated photoelectrochemical performance enhancements. The magnitudes of the effects of Ti incorporation on electronic and magnetic properties appear to be highly synthesis-dependent, which has made difficult the development of consistent and general mechanisms explaining experimental and theoretical observations. In this context, we consider how the electronic structure correlates with Ti impurity incorporation in α -Fe₂O₃ from the perspective of synchrotron-based soft X-ray absorption spectroscopy measurements. Measurements are performed on sets of electrodes fabricated by five relevant and unrelated chemical and physical techniques. The effects of titanium impurities are reflected in the electronic structure through several universally observed spectral characteristics, irrespective of the synthesis techniques. Absorption spectra at the oxygen *K*-edge show that Ti incorporation is associated with new oxygen 2p-hybridized states, overlapping with and distorting the known unoccupied Fe 3d - O 2p band of α -Fe₂O₃. This is an indication of mixing of Ti s and d states in the conduction band of α -Fe₂O₃. A comparison of spectra obtained with electron and photon detection shows that the effects of Ti incorporation on the conduction band are more pronounced in the near-surface region. Titanium *L*_{2,3}-edge absorption spectra show that titanium is incorporated into α -Fe₂O₃ as Ti⁴⁺ by all fabrication methods, with no long-range titania order detected. Iron *L*_{2,3}-edge absorption spectra indicate that Ti incorporation is not associated with the formation of any significant concentrations of Fe²⁺, an observation common to many prior studies on this material system.

Keywords: oxide, solar energy, hematite, X-ray absorption spectroscopy, photoelectrochemistry, solar water splitting

1. Introduction

This article considers the influence of titanium impurity incorporation on the photoelectrochemical performance and electronic structure of hematite (α -Fe₂O₃) photoanodes for solar fuel synthesis.^{1,2,3,4,5,6,7,8,9} A review of prior work on this material system is presented, drawing conclusions from photoelectrochemical experiments and theoretical predictions. We then present new synchrotron-based electronic structure measurements on Ti-modified α -Fe₂O₃ electrodes (referred to in this article as Ti: α -Fe₂O₃), fabricated by five relevant synthetic methods: physical vapor deposition by pulsed laser deposition,¹⁰ atomic layer deposition,¹¹ sol-flame synthesis,¹² all-alkoxide sol-gel synthesis, and aqueous chemical growth.¹³ These results are interpreted and generalized in the context of the existing literature. The comparison of the electronic states resulting from

different synthesis methods is aimed at fostering a rational design of improved active oxide electrodes for photoelectrochemical cells.

Oxide photoelectrodes can be designed to enable the generation of chemical fuels because they facilitate, with high stability, light absorption, charge separation, and electrochemical reactions in solar fuel synthesis devices.^{14,15,16} For synthetic fuels, α -Fe₂O₃ is most importantly applied in photoelectrochemical (PEC) cells to enable the photo-oxidation of water, an anodic electrochemical reaction. That is, at minimum four electrons are injected from an aqueous electrolyte into a solid state α -Fe₂O₃ electrode, yielding oxygen gas as a reaction product. Driving the water oxidation reaction efficiently is a key technological hurdle impeding the development of devices enabling generation of renewable fuels,

such as hydrogen from water reduction or hydrocarbons from carbon dioxide reduction.

In general, photoelectrochemical devices involving transition metal oxides can be made more efficient through electrode modifications that increase the mobility, concentration, and/or lifetime of charges participating in electrochemical reactions.¹⁷ For α -Fe₂O₃, a d⁵ transition metal oxide charge-transfer insulator, these quantities are orders of magnitude lower than those measured for oxides with unfilled¹⁸ or mostly-filled d orbitals.¹⁹ Incorporation of cations into α -Fe₂O₃ has been shown to influence PEC performance through a number of mechanisms, including for example alteration to lattice parameters (trivalent cations),²⁰ increase of carrier concentration (tetravalent and pentavalent cations),²¹ and suppression of recombination through increased electric field near the electrode–electrolyte interface.²²

Titanium incorporation is a known correlate to efficiency enhancement in α -Fe₂O₃ photoanodes. As will be discussed here, numerous mechanisms have been proposed in the literature to explain the observed correlation. Developing a cohesive explanation for performance enhancement has been complicated by the observation that Ti incorporation strongly influences the morphology of resultant films. Morphological effects are not easily decoupled from data in PEC studies. In addition, the synthesis conditions appear to strongly influence the effect of Ti incorporation on performance and physical properties, since the growth parameters dictate the formation of non-innocent, electronically active defects. Some groups suggest that the mechanism in some way involves titanium's role in improving the collection of majority carriers (electrons) at the back contact of the electrode, thereby reducing electron-hole recombination, a process that competes directly with the surface electrochemical reaction of holes in α -Fe₂O₃ anodes.²³

Electron conduction in hematite is known to occur *via* the small polaron hopping mechanism at room temperature.²⁴ Due to significant electron-phonon coupling, conductivity involves the transport of the electron and its polarized local structure (polaron), which has a considerably higher effective mass than a free electron. The conductivity enhancement associated with Ti incorporation has often been suggested to result from substitutional Ti⁴⁺, which when introduced into the α -Fe₂O₃ lattice generates equivalent concentrations of Fe²⁺ to maintain the average charge per cation of +3. The additional electrons associated with Fe²⁺ ions could exist as free carriers for surrounding Fe³⁺ ions, or alternatively remained trapped and therefore yield no conductivity/photocurrent enhancement.²⁵

However, there is evidence suggesting significant Fe²⁺ concentrations are not required for activity enhancement. These characteristics are noted in a comprehensive evaluation (discussed in more detail below) of the transport properties of Ti-doped α -Fe₂O₃ epitaxial films grown by molecular beam epitaxy,²⁴ which are consistent with the room temperature small polaron hopping mechanism. Notably in this study conductivity enhancements are dependent on fabrication conditions, where slow growth rates were found to be associated with cation vacancies, inducing electron donor compensation and yielding highly resistive samples.²⁴

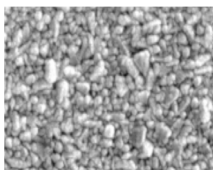
However, it has been noted²⁷ that conductivity enhancements and reduced ohmic drop across electrodes cannot alone explain the efficiency enhancement associated with Ti modification. Ref 27 considers a hypothetical one micrometer thick, highly resistive film ($\rho \sim 10^5 \Omega \cdot \text{cm}$). If this photoelectrode were operating at the theoretical maximum efficiency, corresponding to complete absorption and conversion of light whose energy exceeds the bandgap energy, the potential drop across the film is only 100 mV.²⁷ In contrast to this modest potential drop, in the literature the PEC performance improvement associated with Ti incorporation is much more notable. In the following sections, we discuss select experimental work from the literature and describe major explanations given for solar device performance enhancement associated with Ti incorporation.

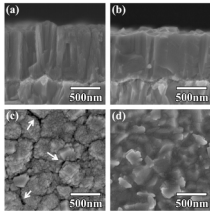
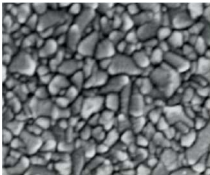
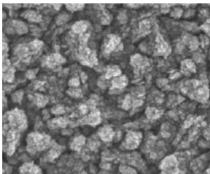
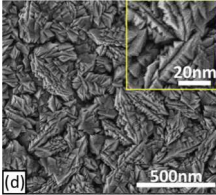
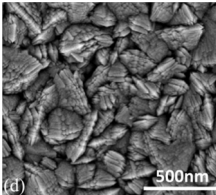
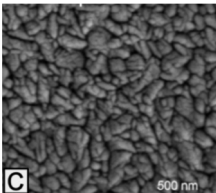
2. Prior experimental work

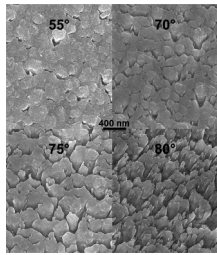
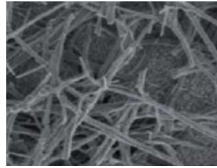
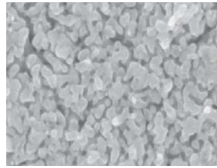
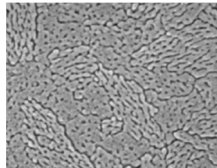
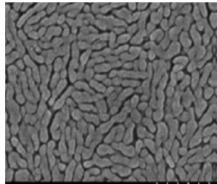
2.1 Materials synthesis and photoelectrochemistry

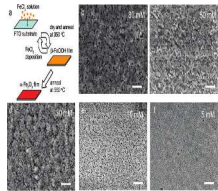
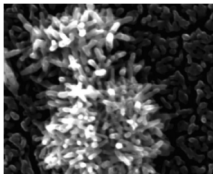
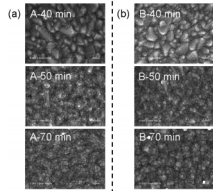
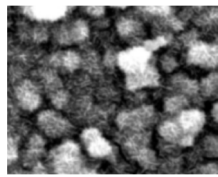
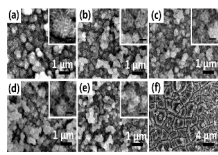
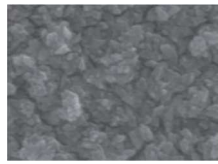
Table 1 provides an overview of select studies on photoelectrochemical behavior of Ti: α -Fe₂O₃ photoanodes, organized by synthesis technique. The table indicates the synthesis technique, provides a representative image of the electrode morphology on the mesoscale, and lists corresponding relevant PEC performance metrics. Major conclusions from these works are summarized below. As above, we adopt the notation Ti: α -Fe₂O₃ to refer to all samples, regardless of whether they are *doped* in the sense as classically understood in the semiconductor physics terminology. For details, including in some cases the optimum dopant concentrations, readers are referred to the individual studies. Typical optima are in the range of 1-10 atomic percent Ti.¹¹

Table 1. Literature survey of photoelectrochemical studies of Ti: α -Fe₂O₃ photoanodes (sorted by synthesis technique). The synthesis technique, representative scanning electron micrographs and corresponding PEC performance metrics are included.

Sample	Fabrication	Thin film texture	Photoelectrochemistry	Ref
Ti: α -Fe ₂ O ₃	Pulsed deposition	laser 	Photocurrent density: 0.5 mAcm ⁻² at 0.6 V vs. Ag/AgCl; IPCE: 15% at 360 nm at 0.6 V vs. Ag/AgCl; Electrolyte: 0.1 M NaOH (pH = 13)	28

Ti: α -Fe ₂ O ₃	Pulsed deposition	laser		Photocurrent density: 2.1 mAcm ⁻² at 0.7 V vs. Ag/AgCl; Electrolyte: 1 M NaOH	29
Ti: α -Fe ₂ O ₃	Atomic deposition	layer		Photocurrent density: 0.8 mAcm ⁻² at 1.8 V vs. RHE; IPCE: 25% at 400 nm at 1.8 V vs. RHE; Electrolyte: 0.1 M phosphate buffer + 200 mM KCl (pH = 6.9)	11
Ti: α -Fe ₂ O ₃	Atomic oxygen assisted molecular beam epitaxy	None		Photocurrent density: approx. 2.3 mAcm ⁻² at 0.8 V vs. Ag/AgCl; IPCE: approx. 6.4% at 350 nm at 0.6 V vs. Ag/AgCl; Electrolyte: 0.1 M NaOH (pH = 13)	60
Ti: α -Fe ₂ O ₃	Atomic oxygen assisted molecular beam epitaxy	None		Photocurrent density: 8 mAcm ⁻² at 0.6 V vs. Ag/AgCl; IPCE: 15% at 360 nm at 0.6 V vs. Ag/AgCl; Electrolyte: 0.1 M NaOH	31
Ti: α -Fe ₂ O ₃	Atmospheric pressure chemical vapor deposition			Photocurrent density: 1.0 mAcm ⁻² at 0.6 V vs. Ag/AgCl; IPCE: 27.2% at 400 nm at 0.6 V vs. Ag/AgCl; Electrolyte: 1 M NaOH (pH = 13.6)	37
Ti: α -Fe ₂ O ₃	Radio frequency magnetron co-sputtering			Photocurrent density: 13 μ Acm ⁻² at 0.3 V vs. Ag/AgCl; IPCE: 3.5% at 400 nm at 0.3 V vs. Ag/AgCl; Electrolyte: 1 M NaOH (pH = 13.6)	26
Mg,Ti: α -Fe ₂ O ₃	Radio frequency reactive co-sputtering			Photocurrent density: \sim 20 μ Acm ⁻² at 0.6 V vs. Ag/AgCl; IPCE: 3.2% at 400 nm at 0.6 V vs. Ag/AgCl; Electrolyte: 1 M Na ₂ SO ₄	38
Ti: α -Fe ₂ O ₃	Reactive magnetron sputtering	DC		Photocurrent density: 0.75 mAcm ⁻² at 0.5 V vs. SCE; IPCE: 14% at 400 nm at 0.5 V vs. SCE; Electrolyte: 1 M NaOH (pH = 13.6)	27

Ti: α -Fe ₂ O ₃	Reactive deposition	ballistic		Photocurrent density: 585 μAcm^{-2} at 1.4 V vs. RHE; IPCE: 31% at 360 nm and 1.4 V vs. RHE; Electrolyte: 1.0 M KOH (pH = 13.6)	22
Ti: α -Fe ₂ O ₃	Solution growth and electrodeposition;			Photocurrent density: 0.67 mAcm^{-2} at 1.23 V vs. RHE; Electrolyte: 1.0 M KOH (pH = 13.6)	40
Ti: α -Fe ₂ O ₃	Electrodeposition;			Photocurrent density: 1.4 mAcm^{-2} at 1.23 V vs. RHE; IPCE: 25% at 330 nm at 1.5 V vs. RHE; Electrolyte: 1.0 M KOH	41
Ti: α -Fe ₂ O ₃	Spray deposition	pyrolysis		Photocurrent density: 1.98 mAcm^{-2} at 0.5 V vs. SCE; Solar to hydrogen conversion efficiency: 1.38% at 0.5 V vs. SCE; Electrolyte: 1 M NaOH (pH = 13.6)	43
Ti: α -Fe ₂ O ₃	Spray deposition	pyrolysis	None	Photocurrent density: 4.05 mAcm^{-2} at 0.45 V vs. NHE; Electrolyte: 1.0 M NaOH (pH = 13.6)	44
Al,Ti: α -Fe ₂ O ₃	Spray deposition	pyrolysis	None	Photocurrent density: 4.38 mAcm^{-2} at 0.45 V vs. NHE; IPCE: 25% at 400 nm at 0.7 V vs. NHE; Electrolyte: 0.1 M NaOH	44
Zn,Ti: α -Fe ₂ O ₃	Spray deposition	pyrolysis	None	Photocurrent density: \sim 3.8 mAcm^{-2} at 0.45 V vs. NHE; Electrolyte: 0.1 M NaOH	44
Ti: α -Fe ₂ O ₃	Ultrasonic pyrolysis	spray	None	Photocurrent density: 1.06 mAcm^{-2} at 0.6 V vs. Ag/AgCl; IPCE: 22% at 365 nm at 0.6 V vs. Ag/AgCl; Electrolyte: 1.0 M NaOH (pH = 13.6)	45
Si,Ti: α -Fe ₂ O ₃	Ultrasonic pyrolysis	spray	None	Photocurrent density: 2.15 mAcm^{-2} at 0.6 V vs. Ag/AgCl; IPCE: 34% at 365 nm at 0.6 V vs. Ag/AgCl; Electrolyte: 1.0 M NaOH (pH = 13.6)	45
Ti: α -Fe ₂ O ₃	Sol-gel method			Photocurrent density: 103 μAcm^{-2} at 0.2 V vs. SCE; IPCE: 32.6% at 400 nm at 0 V vs. SCE; Electrolyte: 1.0 M NaOH (pH = 13.6)	46

Ti: α -Fe ₂ O ₃	Deposition-annealing process		Photocurrent density: 2.80 mAcm ⁻² at 1.23 V vs. RHE; IPCE: 22% at 350 nm at 1.02 V vs. RHE; Electrolyte: 1.0 M NaOH (pH = 13.6)	47
Ti: α -Fe ₂ O ₃	Hydrothermal method		Photocurrent density: 1.91 mAcm ⁻² at 1.23V vs. RHE; IPCE: 60% at 350 nm at 1.53 V vs. RHE; Electrolyte: NaOH (pH = 13.6)	49
Ti: α -Fe ₂ O ₃	Hydrothermal method		Photocurrent density: ~0.6 mAcm ⁻² at 0.2 V vs. SCE; Electrolyte: NaOH (pH = 13.6)	50
Ti: α -Fe ₂ O ₃	Hydrothermal method		Photocurrent density: 0.15 mAcm ⁻² at 1.23 V vs. RHE; Electrolyte: 1 M NaOH (pH = 13.6)	52
Ti: α -Fe ₂ O ₃	Hydrothermal method; in situ solid-state reaction method		Photocurrent density: 1.2 mAcm ⁻² at 1.23 V vs. RHE; Electrolyte: 1 M NaOH (pH = 13.6)	53
Ti: α -Fe ₂ O ₃	Hydrothermal method		Photocurrent density: 0.66 mAcm ⁻² at 1 V vs. Ag/AgCl; IPCE: 27% at 360 nm at 1.23 V vs. RHE; Electrolyte: 0.5 M NaCl (pH 6.7)	58

The morphological, optical, and photoelectrochemical properties of Ti: α -Fe₂O₃ films fabricated on fluorinated SnO₂ substrates (FTO) by pulsed laser deposition (PLD) have been reported.²⁸ The results suggested that the efficiency of electron transport to the back contact is a critical parameter influencing photoelectrochemical performance. In this study, denser electrodes deposited at 300 °C were significantly more efficient than porous electrodes deposited at 23 °C, despite their apparent increased surface area. Lee *et al.* used PLD to fabricate Ti: α -Fe₂O₃ electrodes with a column-like porous nanostructure.²⁹ It was found that the porosity and related photoelectrochemical performance could be modified by controlling the kinetic energy of the ablated species, through variation of deposition background pressure.

Atomic layer deposition (ALD) enables control of the morphology and thickness of the α -Fe₂O₃ films as well as the concentration and distribution of Ti atoms. Zandi *et al.* used ALD to deposit a uniform thin film of Ti: α -Fe₂O₃ as an electrode

on FTO substrates, and compared its PEC performance with that of an undoped α -Fe₂O₃ electrode. It was shown that incorporation of a relatively large percentage of Ti impurities into α -Fe₂O₃ electrodes dramatically enhanced the PEC water oxidation performance.¹¹ This performance enhancement was attributed to a combination of improved bulk material properties (resulting in increased hole collection length) and surface properties (resulting in increased water oxidation efficiency). These property modifications were stated to result from resurrection of a dead layer and a dead surface, respectively, by the Ti impurity atoms. Alternate conditions for atomic layer deposition of Ti: α -Fe₂O₃ have been reported recently.³⁰

It was demonstrated that molecular beam epitaxy assisted by atomic oxygen is also a suitable technique to fabricate controlled epitaxial undoped and Ti-doped α -Fe₂O₃ films as photoanodes for solar water splitting.^{31,32,33} For α -Fe₂O₃(0001) thin films grown on Pt(111) single crystalline substrates, Ti doping was shown to induce a slight modification of the oxygen octahedron

by substituting for Fe^{3+} in the hematite lattice. Improvement of PEC properties in the Ti-doped sample was attributed to an increase of electrical conductivity, induced by a shift of the Fermi level in the doped sample.³³

Chemical vapor deposition (CVD) techniques, including AACVD (aerosol-assisted chemical vapor deposition) and APCVD (atmospheric pressure chemical vapor deposition), have been used to prepare undoped and Si- and Ti-doped $\alpha\text{-Fe}_2\text{O}_3$ nanostructures.^{34,35,36} It was recently reported that photoelectrochemically active Ti: $\alpha\text{-Fe}_2\text{O}_3$ thin films with preferred crystallographic growth along the (110) direction were successfully synthesized by APCVD. The Ti concentration could be controlled by varying the delivery rate of $\text{Fe}(\text{CO})_5$ and TiCl_4 precursors.³⁷ A maximum efficiency was observed at ~ 0.8 atom% Ti in hematite, with the incident photon conversion efficiency (IPCE) measured in alkaline electrolyte to be a high value of 27.2% under an applied bias of 0.6 V vs. Ag/AgCl at 400 nm for water splitting. The PEC performance improvement associated with Ti was related to enhanced electric conductivity, beneficial feature sizes, and reduced trap state density in the lattice.

Tang *et al.* reported on the synthesis of pure and Ti-doped $\alpha\text{-Fe}_2\text{O}_3$ thin films by radio frequency (RF) magnetron co-sputtering of iron oxide and titanium targets in Ar/O_2 ambient conditions.²⁶ The Ti concentration in Ti-doped films was controlled by varying the RF power to the titanium target. It was demonstrated that the photoresponse of Ti: $\alpha\text{-Fe}_2\text{O}_3$ was improved as compared to the pure $\alpha\text{-Fe}_2\text{O}_3$ films, and the flatband potentials were negatively shifted toward more favorable potentials for water splitting. The performance improvements were attributed to enhanced conductivity due to increased donor concentrations and improved crystallinity. In a later study, using the same method they successfully prepared charge-compensated Ti and Mg co-doped $\alpha\text{-Fe}_2\text{O}_3$ thin films.³⁸ It was suggested that the charge-compensated donor-acceptor co-doping can lead to increased electron mobility, optimized electrical conductivity, as well as reduced carrier recombination. As a result, the Ti and Mg co-doped $\alpha\text{-Fe}_2\text{O}_3$ thin films exhibited significantly enhanced PEC performance as compared to pure and solely Ti-doped $\alpha\text{-Fe}_2\text{O}_3$ thin films. Co-doped systems involving Ti have also been explored by combinatorial methods.³⁹ Ti: $\alpha\text{-Fe}_2\text{O}_3$ thin film electrodes for PEC water splitting have been prepared by Glasscock *et al.* using reactive DC magnetron sputtering.²⁷ Ti: $\alpha\text{-Fe}_2\text{O}_3$ exhibited larger photocurrent as well as lower onset potential than the undoped material, which was explained by the improved electrical conductivity, the lowered activation energy, and the increased charge carrier density induced by Ti doping.

Hahn *et al.* demonstrated the preparation and optimization of nanostructured Ti: $\alpha\text{-Fe}_2\text{O}_3$ thin films using the reactive ballistic deposition (RBD) technique, and studied their physical, chemical, and PEC properties.²² They found that manipulating the deposition angle had a strong effect on the PEC water oxidation performance of the films. A nanocolumnar morphology and beneficial porosity was attained using glancing angles, which improved the relative conversion of visible-light photons when compared to dense films deposited at normal incidence. The increased PEC efficiency brought about by Ti^{4+}

doping was attributed to both the improvement of electron transport within the bulk of the film and the suppression of recombination at the film-electrolyte interface due to an increased electric field strength near the surface.

Franking *et al.* reported an approach to perform post-growth doping of $\alpha\text{-Fe}_2\text{O}_3$ nanowires by depositing a Ti precursor solution, followed by annealing in air.⁴⁰ It was found that the Ti-treatment increases the donor concentration of hematite by tenfold and generally facilitates majority carrier transport and collection, which may account for the performance enhancement. This post-growth doping method was also applied by Wang *et al.* to other $\alpha\text{-Fe}_2\text{O}_3$ nanostructures, for example to electrochemically deposited nanoporous $\alpha\text{-Fe}_2\text{O}_3$ films.⁴¹ The Ti-treated samples exhibited comparably high photoresponse, which could be attributed to a combined Ti/Sn doping effect, the latter caused by thermal diffusion of Sn from the FTO substrate during the annealing process. Hu *et al.* used electrochemical deposition to synthesize Ti: $\alpha\text{-Fe}_2\text{O}_3$ by co-deposition using FeCl_3 and titanium isopropoxide precursors.⁴² Here also a solution of CoF_3 was used to modify the surface of photoanodes to negatively shift the flat-band potential.⁴²

Ti: $\alpha\text{-Fe}_2\text{O}_3$ films were deposited by a spray-pyrolysis deposition (SPD) method. The morphology was observed to be nanoporous, and porosity increased with increasing impurity concentration.⁴³ The significantly enhanced PEC performance was attributed to a combination of the modified nanoporous surface morphology, suitable bandgap, and increased donor density induced by Ti doping. When compared to solely Ti-modified $\alpha\text{-Fe}_2\text{O}_3$ films, greater photocurrent enhancement was observed following the addition of either Al^{3+} or Zn^{2+} in conjunction with Ti^{4+} during the SPD process.⁴⁴ Simultaneous doping of Ti^{4+} (5%) and Al^{3+} (1%) resulted in the largest photoactivity, with the IPCE measured to be 25% at 400 nm and 0.7 V vs. NHE. Co-doping with Zn^{2+} also showed promise since the onset potential was cathodically shifted by ~ 0.22 V. Zhang *et al.* conducted a systematic study on the PEC performance of undoped, Si-doped, Ti-doped, and co-doped $\alpha\text{-Fe}_2\text{O}_3$ films prepared by ultrasonic spray pyrolysis (USP).⁴⁵ Si and Ti co-doping was found to balance the ion radius difference between Fe^{3+} and Si^{4+} or Ti^{4+} as well as increase the donor concentration. This resulted in a measured IPCE of 34% at 365 nm and 0.6 V vs. Ag/AgCl for the co-doped film, much higher than 10%, 20%, and 22% for the undoped, Si-doped, and Ti-doped films, respectively.

Ti: $\alpha\text{-Fe}_2\text{O}_3$ thin films were prepared on FTO substrates by the sol-gel route.⁴⁶ Titanium in the $\alpha\text{-Fe}_2\text{O}_3$ lattice was suggested to increase the conductivity and the carrier density of the thin film, with IPCE reaching 32.6% at 400 nm without any additional potential vs. SCE. Wang *et al.* reported a new deposition-annealing (DA) process for preparing highly photoactive Ti: $\alpha\text{-Fe}_2\text{O}_3$ films by adding titanium butoxide as a Ti precursor into an iron chloride solution during synthesis.⁴⁷ Compared to the un-modified sample, the photocurrent onset potential of Ti: $\alpha\text{-Fe}_2\text{O}_3$ was shifted about 0.1-0.2 V to lower potential, and the optimized film achieved relatively high photocurrent density (1.83 mA cm^{-2}) and IPCE values (1.02 V vs RHE). The enhanced photocurrent was attributed here to increased donor density and reduced electron-hole

recombination at a timescale beyond a few picoseconds, as a result of Ti doping. This DA process was subsequently used to examine the effect of electrochemical pretreatment on Ti: α -Fe₂O₃ electrodes.⁴⁸

Ti: α -Fe₂O₃ nanostructures with an urchin-like morphology were synthesized by Deng *et al.* by adding TiCN as a Ti precursor in a hydrothermal process at 95 °C.⁴⁹ The presence of Ti greatly enhanced the plateau photocurrent to a remarkable value of 3.76 mA cm⁻², with high IPCE of 60% measured at 350 nm and 1.53V vs. RHE. The high PEC performance with Ti modification was attributed the favorable urchin-like morphology, increasing the effective surface area, reduced electron-hole recombination, and increased donor density. Recently, TiCl₄ was used as the Ti precursor for the synthesis of Ti: α -Fe₂O₃ films in a hydrothermal process.^{50,51} In the study by Cao *et al.*⁵⁰ the hydrothermal growth process, Ti⁴⁺ was found to be associated with thicker films and increased carrier concentrations. It was further suggested that the increase of carrier concentrations, rather than morphology change or surface passivation, played the primary role in the photocurrent improvement after doping. Micro-nano-structured α -Fe₂O₃ films were synthesized by Miao *et al.* through a simple hydrothermal method at 100 °C using a TiCl₄ ethanol solution as the Ti precursor.⁵² It was believed that Ti impurities enhanced the electrical conductivity and facilitated the separation and transport of electrons and holes. Later, the same group showed results where a higher concentration of Ti ions (up to 19.7% by atomic ratio) was incorporated into hydrothermally grown Ti-doped (2.2%) films by an in situ solid-state reaction method.⁵³ It was suggested that the higher Ti concentration led to a dramatic improvement of the electrical conductivity of the micro-nanostructured film, which enhanced the photocurrent eight-fold. High temperature solid state reactions are another avenue for synthesis: Balko and Clarkson⁵⁴ fabricated Ti,Sn: α -Fe₂O₃ pellets using a ceramic technique involving TiO₂ and SnO₂ as dopant sources.

It has also been shown recently that Ti can be incorporated into α -Fe₂O₃ by the hydrothermal method when titanium (IV) butoxide is included in the precursor solution,⁵⁵ as well as TiCl₃.⁵⁶ Another study⁵⁷ incorporated Ti through inclusion of titanium carbonitride in the precursor solution. When annealed in an oxygen deficient environment, high photocurrents (4.56 mA cm⁻² at 1.6 V vs. RHE) were achieved. A recently published study from Shen *et al.*⁵⁸ showed photoelectrochemical performance increases significantly when Ti is incorporated through inclusion of TiCl₃ in the precursor solution for hydrothermal growth. Ultrafast transient absorption spectroscopy measurements showed no significant change upon Ti incorporation in the 0 to 1000 ps time scale. This indicates alteration of electron-hole recombination dynamics is not a major effect, although the study does not rule out this effect on longer timescales.⁵⁸

2.2 Model experimental systems

The interpretation of photoelectrochemical data from α -Fe₂O₃ photoanodes is facilitated by results from experiments conducted on model systems, which are typically planar epitaxial films and single crystals. These systems are structurally less complex than state-of-the-art electrodes, and can

be very well characterized, allowing one to draw clear structure-function relationships. References 24 and ⁵⁹ provide such foundational work on the structural and electronic effects of titanium incorporation in α -Fe₂O₃, based on characterization of epitaxial films grown by oxygen-plasma-assisted molecular beam epitaxy (OPAMBE).

In a study on electronic transport,²⁴ Ti⁴⁺ was found to substitute for Fe³⁺ in epitaxial Ti-doped α -Fe₂O₃ thin films [(Ti_xFe_{1-x})₂O₃], for $x \leq 0.09$. For low doping levels, no significant concentrations of Fe²⁺ were found. From X-ray absorption near-edge spectroscopy measurements, it was deduced that Ti substitutes for Fe in the hematite lattice and does not form anatase or rutile titania microstructural regions.

In this study²⁴ two growth rates were examined, which yielded interesting results relevant to our understanding of conduction in Ti: α -Fe₂O₃. First, the transport results for semiconducting films were consistent with the small polaron hopping conduction mechanism at higher temperature, including room temperature, near which PEC cells operate. Films fabricated with a slow growth rate were highly resistive and those with a fast rate were more conductive. Resistivity and Hall measurements on films with a fast growth rate possessed carrier concentrations on the order of 10¹⁹ to 10²⁰ cm⁻³ at room temperature and mobilities of 0.1 to 0.6 V cm⁻². The resistivity in samples from slow growth was attributed to the formation of cation vacancies, which serve to charge compensate donor electrons.²⁴ Based on interpretation of charge balance among the possible species in this system, the authors convincingly argue that the net carrier concentration in their system is given by

$$n - p = [Ti_{Fe}'] - 3[V_{Fe}'''] \quad (\text{Eq. 1})$$

Here, $[Ti_{Fe}']$ is the concentration of ionized substitutional Ti⁴⁺ and $[V_{Fe}''']$ is the concentration of Fe³⁺ vacancies. In this case, cation vacancies are more prevalent in slow growth conditions because the oxygen fugacity is higher during growth.²⁴ This explanation appears consistent with the observation of large variations in the photoelectrochemical effects of Ti incorporation – the concentration of compensating Fe³⁺ vacancies will depend in large part on the fabrication conditions.

A model system aimed at elucidating the magnetic structure of Ti: α -Fe₂O₃ has also been considered.⁵⁹ In Ref 59, the magnetic structures of (Ti_xFe_{1-x})₂O₃ epitaxial films grown by OPAMBE were investigated in detail. Three structural motifs were considered to interpret the experimental results: α -Fe₂O₃ with one substitutional Ti atom, with two Ti atoms positioned across a shared octahedral face, and with two substitutional Ti atoms that straddle a vacant octahedral cavity. These structures from Ref 59 are useful for our perspective on this topic and are shown in Figure 1. The Ti: α -Fe₂O₃ studied in this reference was found to possess a majority phase in which Ti is randomly dispersed throughout the two magnetic sublattices. The donor electrons associated with Ti⁴⁺ substituting for Fe³⁺ were localized on Fe sites. We will discuss the magnetic structure results of this study and others on Ti: α -Fe₂O₃ in greater detail below.

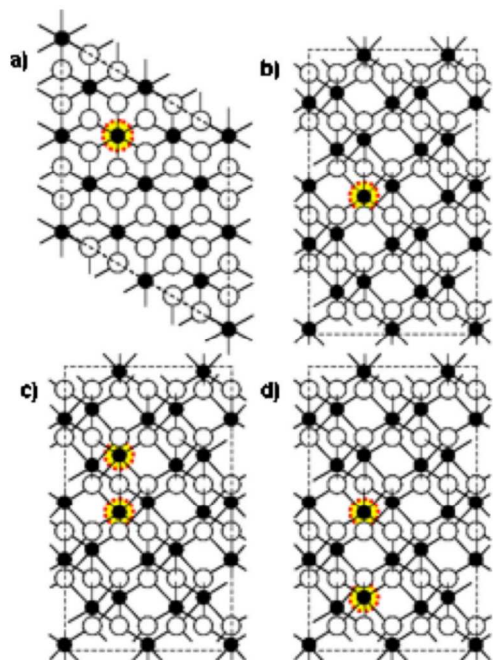


Figure 1. Depictions of Ti substitution scenarios in Ti:α-Fe₂O₃. (a) and (b) One Ti atom substituted for Fe; (c) two substitutional Ti atoms positioned across a shared octahedral face; (d) two substitutional Ti atoms that straddle a vacant octahedral cavity. Black circles represent Fe, white circles represent O, and highlighted black circles represent Ti. From Ref 59.

The model system investigated by Rioult *et al.*⁶⁰ consists of single crystalline Ti:α-Fe₂O₃ deposited epitaxially onto Pt(111) by atomic oxygen assisted molecular beam epitaxy (AO-MBE). The simple geometries of their slab structures allowed investigation of the relationship between required carrier transport lengths and Ti impurity concentrations. Ti incorporation increased the carrier concentrations in the crystals as well as increased the carrier diffusion lengths of *both* electrons and holes.⁶⁰ As in numerous other studies, no Fe²⁺ species were measured by core level spectroscopies. Figure 2 provides a schematic from Ref 60 illustrating the suggested effects of Ti incorporation on carriers' behavior. Here the line thickness is used to convey the strength of the phenomena and band bending is drawn to occur at the α-Fe₂O₃-H₂O interface.

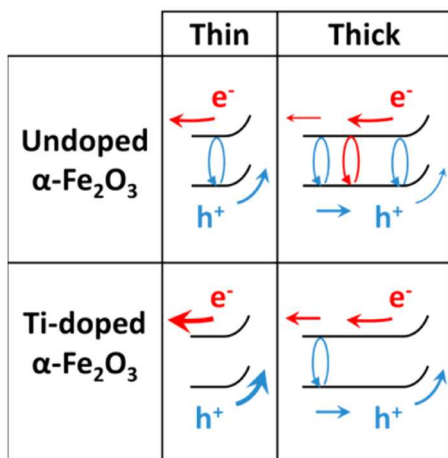


Figure 2. Illustration showing the behavior of electrons and holes in α-Fe₂O₃ and Ti:α-Fe₂O₃ single crystals. From Ref. 60.

Thimsen *et al.*⁶¹ combined experimental synthesis and predictions by density functional theory and a mixed metal oxide band structure method to study Ti-Fe-O materials based on combinations of anatase TiO₂ and α-Fe₂O₃. The materials were synthesized using a premixed flame aerosol reactor. The combined use of theory and experiment was used to develop a method to predict the electronic band structure of mixed metal oxides. It appeared the positions of band extrema were governed more by atomic composition than crystal structure. Specifically the band gap energy of the anatase-based materials decreased with Fe content, until Fe and Ti concentrations were nearly equivalent. Increasing the relative Fe concentration beyond this composition yielded materials with bandgaps equal to that of α-Fe₂O₃.⁶¹ The correlation between film color and DFT-calculated energy gap is shown in Figure 3.

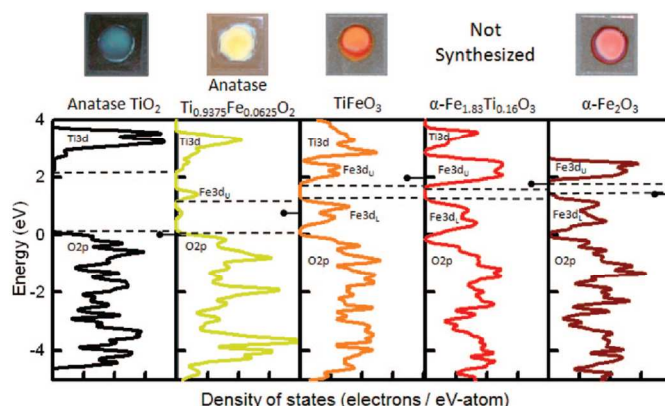


Figure 3. Analyses of materials in the Fe-Ti-O system from the basis materials anatase TiO₂ and α-Fe₂O₃. Images show color of synthesized films and plots show corresponding densities of states from density functional theory calculations, with energy gaps indicated. From Ref. 61.

3. Prior theoretical work

Theoretical calculations of the electronic and magnetic structure of Ti:α-Fe₂O₃ directly inform our interpretation of photoelectrochemical data.^{62,63} Density functional theory (DFT) is the most commonly used method in solid state physics for investigating electronic structures of materials. Applying conventional DFT approximations to α-Fe₂O₃ is complicated by the presence of localized Fe 3d electrons, which, when combined with the necessarily approximate electron exchange-correlation (XC) functionals, gives rise to large errors due to incomplete cancellation of Coulomb and exchange self-interaction terms.⁶⁴ The DFT+U method⁶⁵ replaces the inexact treatment of electron exchange with Hartree-Fock-like intra-atomic Coulomb (U) and exchange (J) interaction terms for the localized d electrons. Since Hartree-Fock theory contains exact electron exchange, the DFT+U method provides a superior description of most mid-to-late first row transition metal oxides and has been adopted for studying α-Fe₂O₃. The complexities are demonstrated in Refs ⁶⁶ and ⁶⁷, which consider the electronic and magnetic properties of Ti:α-Fe₂O₃ using both DFT and DFT+U (U-J = 6.1 eV for both Fe and Ti)⁶⁶ with the local density approximation (LDA) as the XC functional. In their model, one Ti atom substitutes one Fe in a 30-atom or 60-atom cell. Both LDA and LDA+U predict that Ti donates one extra electron and exists as Ti⁴⁺, but they predict

different states for that electron. With LDA, the additional electron donated by the Ti^{4+} impurity is delocalized over the Fe atoms with the moment opposite to that of the substituted Fe atom. This is associated with itinerant d electrons and a metallic band structure, a typical artifact for LDA treatment of such metal oxides. In contrast, LDA+U found that the extra d electron is localized on a single Fe atom.

Huda *et al.* used LDA+U ($U-J = 5.5$ eV for Fe) to study the electronic structure of pure and Ti-doped $\alpha\text{-Fe}_2\text{O}_3$.⁶⁸ One Ti atom substitutes for one Fe in a 30-atom cell. Ti substitution led to a decrease in unit cell volume, which might improve carrier transport by increasing the hopping probability of small polarons. The LDA+U band gap also decreases to 1.19 eV from 1.72 eV for pure $\alpha\text{-Fe}_2\text{O}_3$. This study produced total density of states plots, which are helpful in demonstrating the modification to the $\alpha\text{-Fe}_2\text{O}_3$ valence and conduction bands upon transition metal incorporation (Figure 4). Here, among all 3d transition metal impurities examined in the study, Ti was highlighted to be associated with electronic bands with more dispersive character.⁶⁸ These dispersive Ti bands would lead to a lower effective mass of electrons, and thus could positively influence conductivity and PEC performance.

Liao *et al.* performed generalized gradient approximation (GGA)+U ($U-J = 4.3$ eV for Fe and 5.0 eV for Ti) calculations for Ti substituted $\alpha\text{-Fe}_2\text{O}_3$ (0001) slabs.⁶⁹ One Ti atom substitutes one Fe atom closest to surface on each side of the $\alpha\text{-Fe}_2\text{O}_3$ (0001) slabs. For the stable, fully-hydroxylated termination, there are 29 atoms and 104 atoms in (1x1) and (2x2) slabs, respectively. For the (1x1) slab, the additional electron was predicted to be on the Fe site. For the (2x2) slab, two eigenstates were obtained, with the $\text{Fe}^{3+}/\text{Ti}^{3+}$ case higher in energy by 0.21 eV than the $\text{Fe}^{2+}/\text{Ti}^{4+}$ case. The presence of Ti near the surface shifts the valence band maximum to be less negative, which would be desirable for water reduction on hematite if the band gap value does not change and as a result, the conduction band minimum is shifted by a similar amount. The energetics of water oxidation on pure and doped $\alpha\text{-Fe}_2\text{O}_3$ (0001) slabs were reported. Compared to other dopants (such as Mn, Co) explored, the presence of Ti near the surface does not help reduce the reaction potential required, because the presence of Ti gives rise to too strong binding of some intermediate species while destabilizing the others.

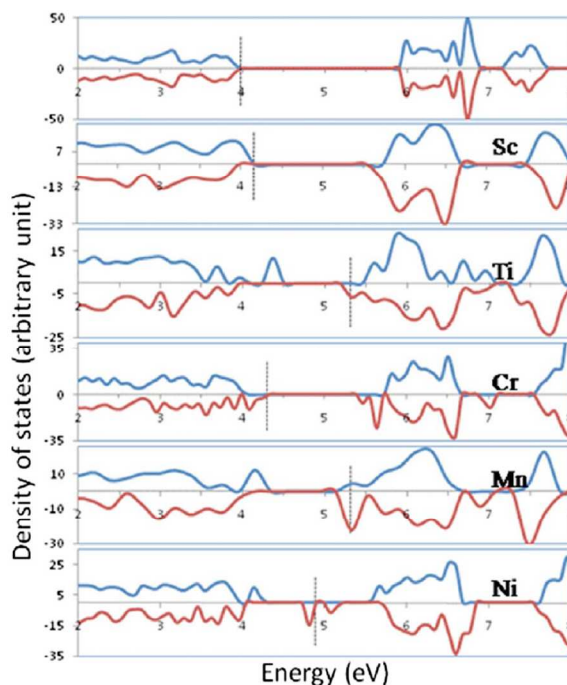


Figure 4. Calculated total electronic density of states for pure $\alpha\text{-Fe}_2\text{O}_3$ and $\alpha\text{-Fe}_2\text{O}_3$ incorporated with Sc, Ti, Cr, Mn, and Ni at substitutional sites. The highest occupied state is indicated by the dashed vertical line in each case. From Ref 68.

In addition to their work using periodic DFT/DFT+U, Liao *et al.*⁷⁰ performed quantum chemistry calculations to investigate the electron transfer process in Ti-doped hematite. For pure $\alpha\text{-Fe}_2\text{O}_3$, the electron carriers are localized Fe 3d electrons. The transport mechanism of hematite was proposed to follow the small polaron model,⁷¹ in which electron hopping is coupled to lattice distortion and results in small mobility. In Liao *et al.*'s study, electron transfer in doped $\alpha\text{-Fe}_2\text{O}_3$ was modeled using electrostatically embedded clusters at the level of unrestricted Hartree-Fock (UHF) theory. Figure 5 shows the free energy curves for electron carriers hopping between Fe and Ti sites in Ti-doped hematite. The free energy is lower when the electron is localized on the Ti site than when the electron is localized on the Fe site. This can be explained by the ionization potentials (IPs) from Ti^{4+} to Ti^{3+} (43.27 eV) and from Fe^{3+} to Fe^{2+} (30.65 eV). The much larger IP from Ti^{4+} to Ti^{3+} suggests that the electron carrier is more strongly attracted to Ti. Therefore, from this perspective Ti is not an ideal dopant for improving electron transport in $\alpha\text{-Fe}_2\text{O}_3$.

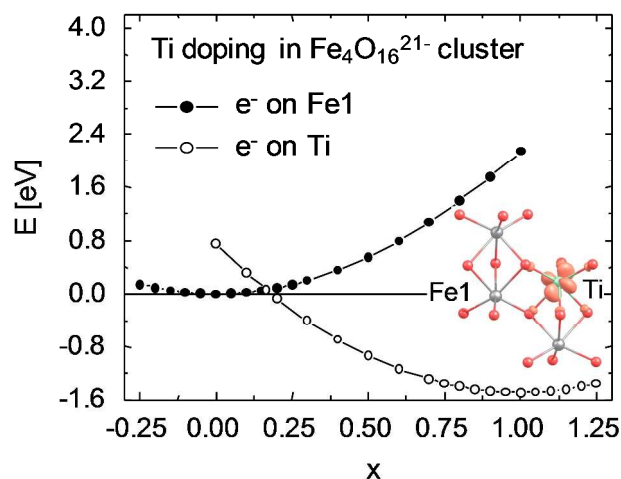


Figure 5. Unrestricted Hartree-Fock (UHF) potential energy curves along the collective nuclear coordinate x for electron transfer between Fe1 and Ti. The energy for $x = 0$ on the left curve is set to zero. The figure within the plot is a density difference isosurface plot of the added electron localized on the Ti site (in green). Fe ions are in grey. O ions are in red. A contour value of 0.14 electrons/ \AA^3 is used. Adapted with permission from P. Liao, M. C. Toroker and E. A. Carter, *Nano Letters*, 11, 1775–1781 (2011). Copyright 2011 American Chemical Society.

4. Magnetic structure

In this section we discuss the magnetic structures of α - Fe_2O_3 and $\text{Ti}:\alpha\text{-Fe}_2\text{O}_3$. Keeping with the theme and motivation of this article, we restrict our brief discussion to those points that may be relevant to solar energy conversion devices.

$\alpha\text{-Fe}_2\text{O}_3$ is a spin-canted antiferromagnetic oxide possessing stacked bilayers of high spin $d^5 \text{Fe}^{3+}$ cations. Along the [001] direction, the spin orientation follows the scheme $\dots O_3\text{-}M_\alpha\text{-}M_\alpha\text{-}O_3\text{-}M_\beta\text{-}M_\beta\text{-}O_3\text{-}M_\alpha\text{-}M_\alpha\text{-}O_3\text{-}M_\beta\text{-}M_\beta\dots$, where M represents a member of the cation bilayer with the α or β spin orientation.⁵⁹ The anisotropic conductivity of $\alpha\text{-Fe}_2\text{O}_3$ is typically explained by the classical model, which predicts ultra-low conductivity in the [001] direction, since a minority spin electron added to a lattice of high-spin $d^5 \text{Fe}^{3+}$ atoms is forbidden by Hund's rule from moving to an adjacent spin-antiparallel Fe^{3+} atom. The anisotropy can be explained in detail by *ab initio* electronic structure calculations and electron transfer theory,⁷² which predict that the lower mobility in the [001] direction than within a - b planes is caused by the larger electronic coupling within the basal plane.

The complex nature of magnetism in $\text{Ti}:\alpha\text{-Fe}_2\text{O}_3$ is evident by contrasting the magnetic structures associated with hematite ($\alpha\text{-Fe}_2\text{O}_3$) and ilmenite (FeTiO_3), the two compositional extrema of the Fe-Ti-O rhombohedral oxide system. FeTiO_3 has the same rhombohedral structure of $\alpha\text{-Fe}_2\text{O}_3$ but alternating Fe bilayers are replaced with Ti^{4+} (a d^0 cation). Remaining Fe exists in the $2+$ oxidation state. Figure 6 illustratively contrasts the magnetic structures of the two materials.⁷³

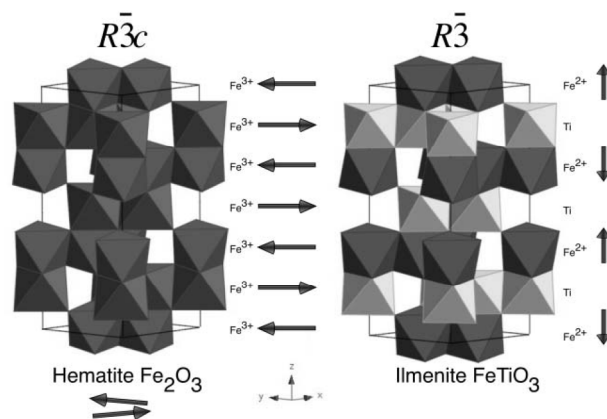


Figure 6. Schematic showing the magnetic structures of $\alpha\text{-Fe}_2\text{O}_3$ below 675 °C (left) and FeTiO_3 below 55 K (right). Dark octahedra contain Fe and light octahedra contain Ti. From Ref. 73.

In the conditions portrayed in Figure 6, in $\alpha\text{-Fe}_2\text{O}_3$ there is a strong antiferromagnetic superexchange between Fe^{3+} spins along [001]. The interaction is mediated by the oxygen layers between Fe bilayers. Antiferromagnetic ordering also exists in FeTiO_3 , but here the interaction between Fe^{2+} spins takes place between two layers of oxygen atoms, since $d^0 \text{Ti}^{4+}$ is not paramagnetic. In contrast to those in $\alpha\text{-Fe}_2\text{O}_3$, the spins in FeTiO_3 are oriented parallel to the hexagonal c axis. As a result of their distinct magnetic structures, $\alpha\text{-Fe}_2\text{O}_3\text{-FeTiO}_3$ solid solutions, as can be found in nature, are known to exhibit interesting magnetic effects.⁷³

Regarding the magnetism associated with intermediate compositions in this rhombohedral system, for example the $\text{Ti}:\alpha\text{-Fe}_2\text{O}_3$ considered here, less is known. Butler *et al.* predicted by first-principles calculations that Ti^{4+} would preferentially substitute for Fe^{3+} in a single magnetic sublattice of $\alpha\text{-Fe}_2\text{O}_3$.⁷⁴ If $d^0 \text{Ti}^{4+}$ substitutes preferentially in a Fe bilayer of one particular spin orientation, then the spin of that layer will be reduced.⁷⁵ In the context of the photoelectrode, we expect by extension this would influence electron transport between Fe bilayers through its effect on the degree of antiferromagnetic ordering along the c -axis. Experimentally, in MBE-grown epitaxial films, a random distribution of Ti impurities was preferred; however approximately 1/8 of the Ti was found to be ordered.⁵⁹

Rivera *et al.*⁷⁶ discussed the magnetism of $\text{Ti}:\alpha\text{-Fe}_2\text{O}_3$ in the context of quantum chemical modeling based on Hartree-Fock theory. The results indicated two interesting phenomena relevant to magnetism in the system. The presence of Ti in the lattice was found to induce electron density population redistribution from the $3d_{yz}$ atomic orbital towards the $3d_{x^2-y^2}$ atomic orbital. In addition, the additional carrier associated with introduction of the Ti impurity was not localized on the Ti site, nor on O atoms or Fe atoms closest to the impurity. It was suggested⁷⁶ that this observation of partial delocalization can explain some differences between experimental and theoretical values for saturation magnetization in $\text{Ti}:\alpha\text{-Fe}_2\text{O}_3$.

We note also that it is possible the introduction of Ti^{4+} into the $\alpha\text{-Fe}_2\text{O}_3$ lattice reduces the overall octahedral symmetry, which has been shown to reduce the magnetic moment of the high-spin state of the Fe^{3+} ion.⁷⁷ More generally, any disruption

of magnetic anisotropy in α -Fe₂O₃ has significant implications for the system's magnetic properties. Above its Morin temperature ($T_M = 263$ K) and below its Neel temperature (948 K $< T_N < 963$ K), bulk α -Fe₂O₃ is a canted antiferromagnet (canting results in a small net magnetic moment and thus weak ferromagnetism),⁷⁸ as discussed above. Below T_M the system undergoes a spin-flip transition and becomes a pure antiferromagnet. However, as the size of α -Fe₂O₃ particles decreases, the Morin temperature decreases and eventually vanishes for particles smaller than 8-20 nm.⁷⁸ For nanoscale systems, superparamagnetic relaxation of the spin lattice and permanent magnetic moments associated with uncompensated surface spins are commonly observed.⁷⁹ Broadly speaking, the size-dependent magnetic behavior can be due to the different distributions of surface and volume spins and spin canting associated with nanoparticles.⁷⁹ In fact, it is known that surface and bulk Fe³⁺ in nanoscale α -Fe₂O₃ have different magnetic structures.⁸⁰ Notably, at low temperatures the coupling between magnetic domains in nanoscale α -Fe₂O₃ can be moderated by the interaction with light.⁸¹ It was proposed that this phenomenon is related to the relative rates of formation, trapping, and recombination of conduction band electrons.⁸¹

5. Soft X-ray absorption spectroscopy of α -Fe₂O₃ thin films and nanostructures

Hematite is a charge-transfer insulator possessing mixed O 2p-Fe 3d valence and conduction bands. The valence band is dominated by O 2p states and the conduction band minimum is dominated by Fe 3d states.⁵⁹ Soft X-ray absorption spectroscopy (XAS) probes the site- and symmetry-selected unoccupied density of states through an electronic transition from a localized core state to a valence state in a transition metal oxide system. Elemental selectivity is obtained through the large energy separation among core levels, and chemical state sensitivity is possible through chemical shifts of the core levels combined with transitions into specific bond orbitals. The dipole nature of the transitions provides symmetry information. The transition matrix element projects unoccupied electronic states onto a specific core level wave function, thereby providing a local density of states.

Oxygen *K*-edge XAS provides information relevant to the characterization of oxide PEC electrodes because in these materials, above the Fermi level empty bands are predominantly metal character hybridized with O 2p character. This is certainly true for α -Fe₂O₃, whose O *K*-edge XAS has been reported extensively.^{82,83,84} In O *K*-edge XAS measurements, we expect that the energy separations between features are equal to corresponding level spacings in the ground state, since the oxygen-derived final states are fairly delocalized and thus not affected much by the O1s core hole.⁸⁵

The transition metal *L*_{2,3}-edge X-ray spectra, on the other hand, exhibit strong interactions between the 3d valence electrons and the 2p core hole, leading to a characteristic multiplet structure. From the positions and intensities of the multiplet lines one can extract the oxidation state, the spin state, and the crystal field induced at the metal atom by the neighboring oxygens.⁸⁵ That provides information relevant to the characterization of PEC photoelectrodes because of its

sensitivity to the chemical state and local environment of metal cations. Cations in 3d transition metal oxides exhibit a diversity of oxidation states, since there is often a small energy difference between the d^n and d^{n+1} configurations.⁸⁶ The metal 2p-to-3d transition probed through the *L*-edge is strong and the 3d electron count is directly related to the oxidation state. Since the character and occupancy of d orbitals are responsible for a large number of the chemical and physical properties of transition metal oxides, a probe of transition metal 2p absorption provides essential information for this application. This is especially true for the Ti: α -Fe₂O₃ system presently considered, since the composition of cations with mixed valence has long been suggested to influence conductivity in doped α -Fe₂O₃.²⁵

From the investigations reviewed above, one deduces the necessity to observe the properties of metal dopants in α -Fe₂O₃ in conditions known to be associated with appreciable changes in photocurrent. Below we show results from soft XAS measurements conducted on α -Fe₂O₃ and Ti: α -Fe₂O₃ photoanodes synthesized by five contrasting techniques. The photoelectrochemical performance influence of Ti in these conditions is either documented here or is documented in published literature. Characterization of this type is used as an initial measure of the rate of the electrochemical water oxidation process. In this work, these data are included to establish that the materials we investigate are photoelectrochemically active, which as discussed below is an important prerequisite for developing electronic structure -- electrochemical activity relationships in materials development. Total electron yields were measured for the samples upon irradiation of the α -Fe₂O₃ electrodes with linearly polarized X-rays from Beamline 8.0 at the Advanced Light Source. The resolutions of the measurements were 0.2 to 0.3 eV. The incident radiation flux was monitored by the photocurrent produced in a gold mesh in the beam path. Total fluorescence yield was monitored simultaneously with total electron yield; for an efficient collection of the fluorescence yield, a channel plate detector with an Al filter was used.

5.1 Thin films fabricated by pulsed laser deposition

Here, we consider α -Fe₂O₃ and Ti: α -Fe₂O₃ thin films fabricated by pulsed laser deposition. Pulsed laser deposition is a vacuum-based thin film deposition technique whereby energetic species are deposited on a heated substrate by species liberated from the pulsed laser ablation of a target material. We first physically characterize the samples deposited by PLD and confirm the activation of Ti impurities for photoelectrochemical applications.

Thin film electrodes were fabricated as described in detail in Ref.⁸⁷ The α -Fe₂O₃ target fabricated for deposition was modified with 1 and 2.5 wt% TiO₂. The resultant film compositions were estimated using energy dispersive X-ray spectroscopy to be approximately 1.1 at% and 3.3 at%, respectively, for the two target compositions. The films were approximately 450 nm thick. For simplicity samples are indicated in this article by their corresponding target composition (*i.e.* 1% or 2.5%). X-ray diffraction patterns (not shown here) indicate the existence of crystalline hematite.

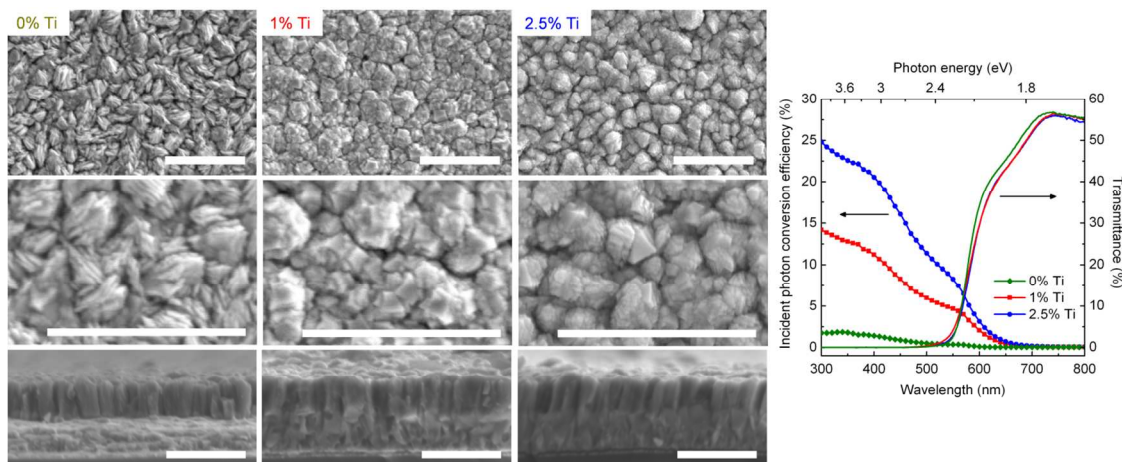


Figure 7. Left: Top-down (top and center panels) and cross section (bottom panels) view scanning electron microscopy images of the thin films deposited by pulsed laser deposition. White scale bars indicate 1 μm . Right: Experimental IPCE spectra with +1 V applied *versus* a Pt counter electrode (0.1 M NaOH aqueous electrolyte, 100 mW cm^{-2} simulated AM1.5 illumination) for un-modified (green), 1% Ti (red), and 2.5% Ti (blue) thin films deposited by pulsed laser deposition. This plot also includes the corresponding spectral transmittance curves for comparison with IPCE spectra.

The inclusion of titanium was found to influence the morphology of the films considerably. Figure 7 provides SEM images for the films, which were deposited under identical conditions. Top-down images (Figure 7, top panels) show that both the shape and size of grains as well as surface morphology is altered by the inclusion of Ti. The morphology-directing properties of Si in $\alpha\text{-Fe}_2\text{O}_3$ have been reported.⁸⁸ Previous studies of magnetron-sputtered $\text{Fe}_2\text{O}_3\text{:Ti}$ films showed that Ti incorporation reduced the grain size significantly.²⁷ Cross-sectional views in Figure 7 show the films develop by the columnar grain growth mode, which is commonly encountered through depositions of this type.⁸⁹

Figure 7 (right hand side) shows the IPCE of $\alpha\text{-Fe}_2\text{O}_3$ and $\text{Ti}:\alpha\text{-Fe}_2\text{O}_3$ fabricated by pulsed laser deposition. The effect of titanium incorporation is to increase photoanodic current at all wavelengths examined. There is no appreciable change in UV-Vis optical absorption upon Ti incorporation (see transmittance curves in Figure 7). The transmittance curves show that the low IPCE at wavelengths greater than 550 nm is partially due to the lack of optical absorption in the spectral range. Based on our assessment of the morphologies in Figure 7, we believe that the large photocurrent enhancement cannot be attributed to any porosity changes with Ti concentration. We observe no trend of decreasing feature size with titanium incorporation, which is the expected relationship between photoelectrochemical activity and

morphology given the known short minority carrier diffusion length in $\alpha\text{-Fe}_2\text{O}_3$.⁹⁰ We therefore find it is reasonable to conclude that the Ti is electronically activated in $\alpha\text{-Fe}_2\text{O}_3$ films fabricated by PLD in a way that is beneficial to photoelectrochemical performance, consistent with other studies.

Figure 8 shows soft X-ray absorption spectra measured on the $\text{Ti}:\alpha\text{-Fe}_2\text{O}_3$ films fabricated by PLD. Figure 8a (top) shows the full spectral range spanning the Fe $L_{2,3}$ -edge (top), as well as a panel resolving the L_3 band (bottom). The Fe $L_{2,3}$ -edge absorption spectrum possesses four main peaks, which originate from spin-orbit and crystal field splitting, as indicated in the figure. The primary difference observed upon introduction of Ti into the $\alpha\text{-Fe}_2\text{O}_3$ film is the reduction in intensity of the first peak (near 708 eV) with respect to the second (near 710 eV). Figure 8b provides O K -edge absorption spectra of $\alpha\text{-Fe}_2\text{O}_3$ over a broad spectral range (top) and over the narrow range spanning the hybridized O 2p - Fe 3d band (bottom). This band is comprised of two primary peaks, which originate from crystal field splitting. The crystal field of the oxygen ligands splits the Fe 3d orbitals into t_{2g} and e_g components in an octahedral geometry. The energy separation between the peaks provides a measure of the crystal field strength. The antibonding orbitals whose wave functions point toward oxygen ions (e_g) lie higher in energy than those whose wave functions point between them (t_{2g}).

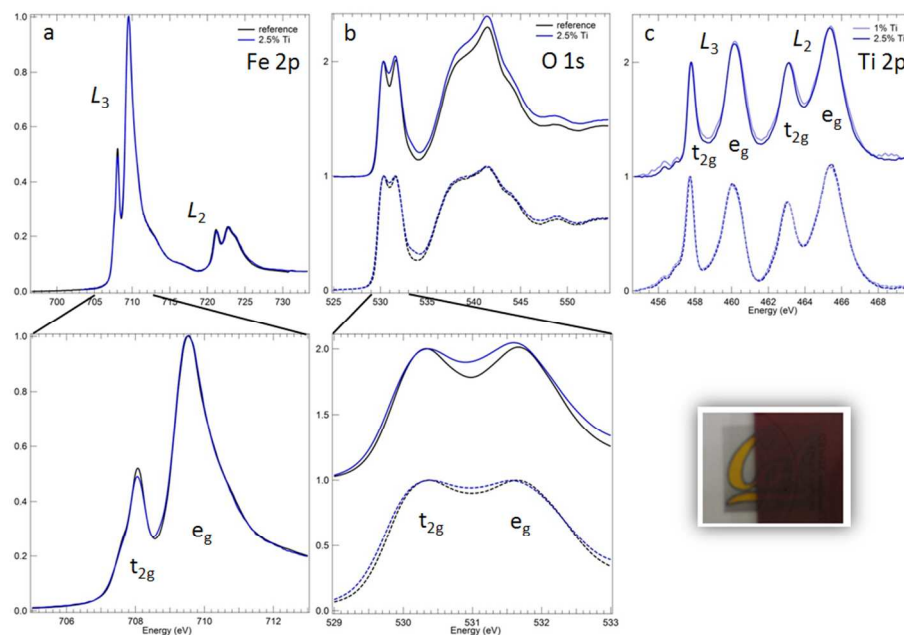


Figure 8. Soft X-ray absorption spectra of α -Fe₂O₃ and Ti: α -Fe₂O₃ thin films fabricated by pulsed laser deposition. (a) Fe $L_{2,3}$ -edge XAS full spectral range (top) and expanded view of L_3 band (bottom). (b) O K -edge XAS full spectral range (top) and expanded view of the O 2p - Fe 3d hybridized region in α -Fe₂O₃. (c) Ti $L_{2,3}$ -edge XAS full spectral range. In all panels, the total electron yield is represented by solid lines and the total fluorescence yield by dashed lines.

With Ti incorporation, there is a higher density of states at energies overlapping with the Fe e_g orbitals. This difference is observable in both electron yield (TEY) and fluorescence yield (TFY), although the difference is greater for TEY. The energy distribution of the additional intensity tends to fill the region between the peaks.

Figure 8c shows Ti $L_{2,3}$ -edge X-ray absorption spectra. Within the noise level the 1% Ti and 2.5% Ti samples are identical, indicating Ti is incorporated with the same charge and with the same local environment in these cases. The energy separation and positions of the four peaks are characteristic of Ti⁴⁺, indicating that titanium is incorporated as Ti⁴⁺ in the electrodes, within the sensitivity of the measurement.

5.2 Thin films fabricated by atomic layer deposition

Next, we present analogous measurements performed on α -Fe₂O₃ thin films fabricated by atomic layer deposition (ALD).¹¹ ALD is a gas phase synthesis technique that offers excellent control over the morphology, thickness and composition of thin film electrodes and can potentially overcome the morphology changes generally induced by doping. The α -Fe₂O₃ films were deposited on FTO substrates by alternating pulses of ferrocene and a combination of water and ozone. Titanium was incorporated in the films by exposing the films to a titanium isopropoxide precursor in between α -Fe₂O₃ ALD cycles. The concentration of Ti atoms in Ti: α -Fe₂O₃ could therefore be controlled by the number of ALD cycles deposited in between Ti deposition. Detailed experimental conditions are provided in Ref 11. Films fabricated in this way have been shown to contain Ti impurities that are activated in the electrode, resulting in

significant performance enhancements in photoelectrochemical measurements.

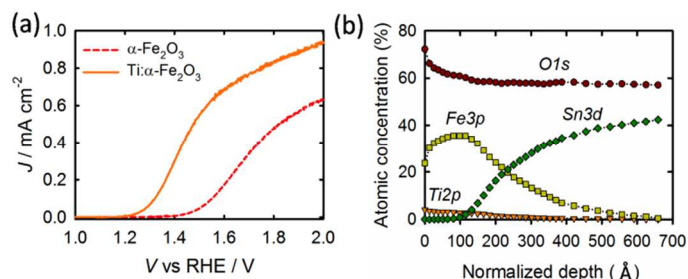


Figure 9. Characterization of α -Fe₂O₃ and Ti: α -Fe₂O₃ thin films fabricated by atomic layer deposition. (a) Photocurrent-potential curves. (b) Atomic concentration depth profiles based on XPS analysis. Adapted from Ref 11.

While the incorporation of any concentration of Ti atoms investigated improved the performance of electrodes of any thickness, an optimal enhancement was found for the thinnest films which contain 1–10% of Ti atoms as measured by XPS depth profiling (Figure 9b). For example, Figure 9a shows the J - V behavior of 36 nm thick α -Fe₂O₃ and Ti: α -Fe₂O₃ films with ~3% Ti. (Figure 9b). It was shown that incorporation of Ti has no measurable effect on light absorption, as was the case for samples in section 5.1. It was also found that Ti incorporation has a negligible effect on the majority carrier density and band edge positions of the photoelectrodes. Through a detailed analysis of the photoelectrochemical (as in Figure 9a) and chemical composition data (as in Figure 9b), the performance improvement was therefore attributed to the activation of a dead layer in the α -Fe₂O₃ thin films by Ti atoms.¹¹

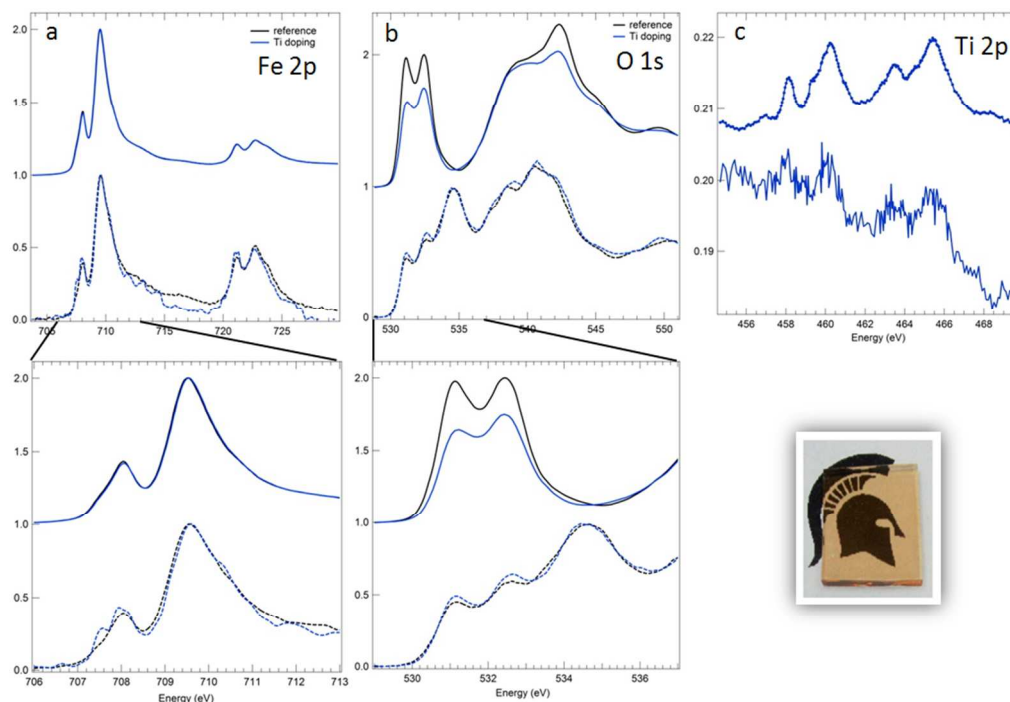


Figure 10. Soft X-ray absorption spectra of α -Fe₂O₃ and Ti: α -Fe₂O₃ thin films fabricated by atomic layer deposition. (a) Fe $L_{2,3}$ -edge XAS full spectral range (top) and expanded view of L_3 band (bottom). (b) O K -edge XAS full spectral range (top) and expanded view of the O 2p - Fe 3d hybridized region in α -Fe₂O₃. (c) Ti $L_{2,3}$ -edge XAS full spectral range. In all panels, the total electron yield is represented by solid lines and the total fluorescence yield by dashed lines.

Figure 10 shows soft X-ray absorption spectra measured on the Ti: α -Fe₂O₃ films fabricated by ALD, as in section 5.1. The same observations made above with respect to the PLD films can be made for the ALD films. The smaller thickness of the ALD films (36 nm) results in weaker fluorescence yields for the Ti 2p absorption (Figure 10c). In addition, the difference in Fe 2p absorption resulting from Ti incorporation is negligible for these thin films. The peak near 535 eV in fluorescence yield O K -edge XAS results from additional states accessible by probing the SnO₂ substrate through the 36 nm film.

5.3 Nanostructure arrays fabricated by sol-flame synthesis

Here, we present analogous measurements performed on Ti: α -Fe₂O₃ nanostructured films fabricated by sol-flame synthesis.⁴ First, arrays of α -Fe₂O₃ nanorods (NRs) with an average length about 350 nm was synthesized on FTO (TEC-8, Pilkington) substrates by air-annealing (550 °C) of hydrothermally grown FeOOH NRs.⁹⁶ Then, the α -Fe₂O₃ NRs were dip-coated with Ti precursor solution (10mM TTIP in IPA) and finally annealed in a 1,000 °C flame for 5 min to enable rapid thermal diffusion of Ti. Figure 11 (left hand side) shows the top-view and cross-sectional SEM images of α -Fe₂O₃ and

Ti: α -Fe₂O₃ nanostructured films fabricated by the sol-flame method. After sol-flame doping, the morphology of NRs remains the same, which enables one to exclude the effect of morphology change on the photoelectrochemical activity. Figure 11 (right hand side) compares the J-V curves of the corresponding four samples. The reference as-grown α -Fe₂O₃ sample does not show significant photocurrent, and the flame-annealed α -Fe₂O₃ sample without Ti impurities shows slightly higher photocurrent. In contrast, the two Ti: α -Fe₂O₃ samples show much higher photocurrent. The sample with higher Ti concentration has double the photocurrent of the sample with lower Ti concentration, which is mainly attributed to the conductivity improvement by the increase of charge carrier density.

Figure 12 shows X-ray absorption measurements, as above in sections 5.1 and 5.2. Here again we observe the characteristic modifications to X-ray absorption spectra induced by Ti incorporation. The O K -edge again shows a low-lying band of unoccupied O 2p states hybridized with Fe 3d states. In this case the changes to the Fe $L_{2,3}$ -edge absorption spectra are more noticeable with fluorescence yield detection.

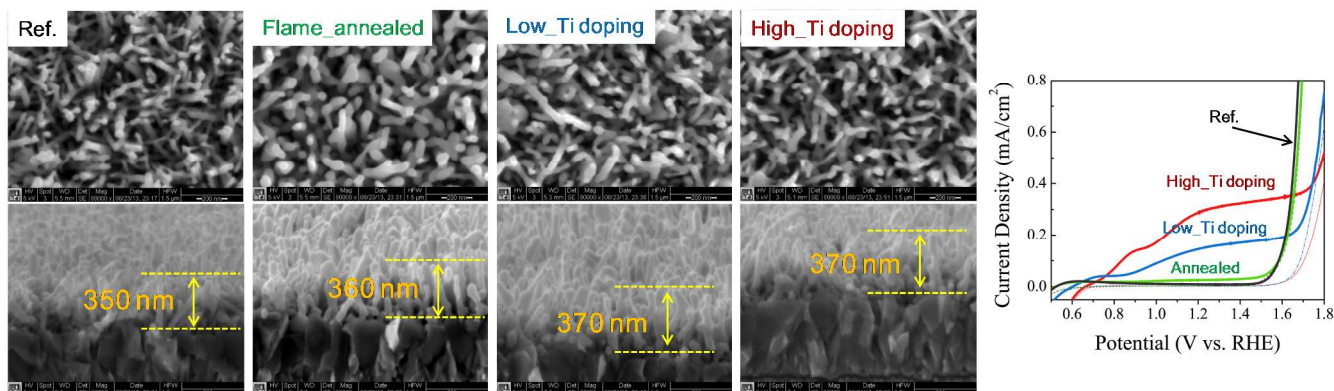


Figure 11. (Left) Scanning electron microscopy images of α -Fe₂O₃ and Ti: α -Fe₂O₃ nanostructured films fabricated by sol-flame synthesis. From left to right: reference sample, flame-annealed sample, annealed + low Ti doping, and annealed + high Ti doping. (Right) J-V curves of four samples [1.0M NaOH electrolyte, AM1.5G simulated solar light (100 mW cm⁻²)]. The sample preparation and sol-flame doping conditions are not optimized.

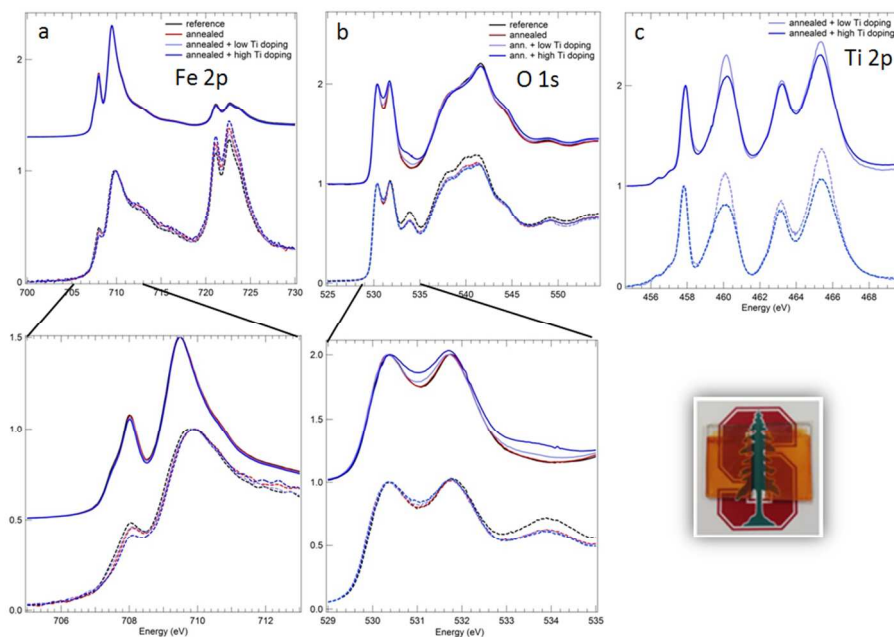


Figure 12. Soft X-ray absorption spectra of α -Fe₂O₃ and Ti: α -Fe₂O₃ thin films fabricated by sol-flame synthesis: as-grown α -Fe₂O₃ (reference sample), flame-annealed α -Fe₂O₃, and two different Ti: α -Fe₂O₃ nanostructured films (a) Fe L_{2,3}-edge XAS full spectral range (top) and expanded view of L₃ band (bottom). (b) O K-edge XAS full spectral range (top) and expanded view of the O 2p - Fe 3d hybridized region in α -Fe₂O₃. (c) Ti L_{2,3}-edge XAS full spectral range. In all panels, the total electron yield is represented by solid lines and the total fluorescence yield by dashed lines.

5.4 Nanostructured films fabricated by the all-alkoxide sol-gel route

Sol-gel and related solution based processes cover a very wide spectrum of precursors and reaction mechanisms during deposition and subsequent heat-treatment to achieve the target films. Consequently the processing temperatures, film structures and qualities vary greatly between the techniques. The best structural control, lowest processing temperatures and highest quality is usually obtained with all-alkoxide based routes where all organics are removed by hydrolysis and evaporation taking place immediately during the deposition in air at room temperature. Such organic-free deposits allow for the important control of the oxidation state, crystallization and elemental homogeneity during the heat-treatment and even greatly extended doping range beyond the thermodynamic limit when the heat-treatment takes place at low temperatures.^{91,92,93,94,95}

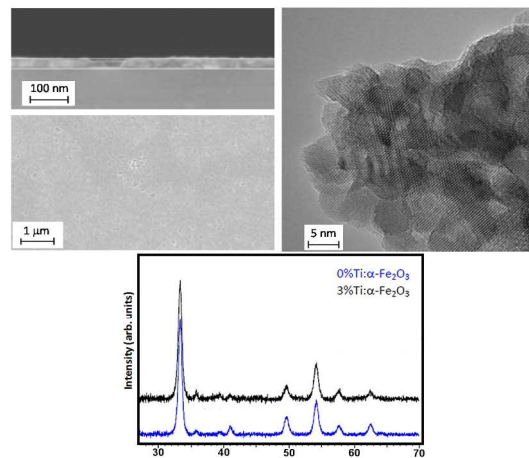


Figure 13. Characterization of 3%Ti: α -Fe₂O₃ films fabricated on Si/SiO₂ by alkoxide sol-gel spin-coating and annealed at 450 °C. Electron microscopy images of the cross-section, surface of the film and fine structure (top) and grazing incidence X-ray diffraction patterns (bottom).

Given these advantages, we investigated the all-alkoxide based sol-gel route for preparation of Ti: α -Fe₂O₃. Films of 0 and 3% metal atom Ti were fabricated by spin-coating at 3000 rpm, 30 s, using 0.3M (metal) Fe(III)-methoxy-ethoxide and Ti(OPr)¹₄ toluene - methoxy-ethanol solutions on a variety of substrates including; Si/SiO₂, Si/SiO₂/Pt, α -Al₂O₃ (0001) and glass/FTO. The oxide films obtained by heating air to 450 and 600 °C at 20 °Cmin⁻¹, were all shiny red and visually without defects. Grazing Incidence X-ray diffraction (GI-XRD) showed that the films consisted of the α -Fe₂O₃ phase as shown in Figure 13. No difference in cell-dimension could be discerned between the Ti: α -Fe₂O₃ and α -Fe₂O₃ films. High resolution SEM imaging of films obtained at 450 °C showed that the films were quite smooth and homogeneous over large areas. However, there were also numerous nano-scale lines and pores, typically in sizes below 20 nm in the films consisting of approximately 5-7 nm sized crystallites. An overview of the film surface is shown in Figure 13. The microstructural differences between the doped and non-doped films were quite small, but discernible in the lesser porosity and stronger coalescence between the crystallites in the latter. The substrate was not found to influence the film microstructure. Cross-section imaging of a cracked film heated to 450 °C on a Si/SiO₂ substrate showed that the film thickness was about 35 nm, which was also corroborated by the TEM study of a film removed from Si/SiO₂/Ti substrate.

TEM studies of films scraped off Si/SiO₂/Ti substrates showed that films heated to 450 °C consisted of densely packed *ca.* 5-7 nm sized crystallites of α -Fe₂O₃ with no amorphous parts, as shown in Figure 13. The Ti incorporation was homogeneous according to the EDS analyses made with a *ca.* 10-15 nm probing beam (the sample was damaged at the point of analysis, but it is believed that the analyses give a fair estimation of elemental homogeneity). Films heated to 600 °C showed increased crystallite sizes, of approximately 10-20 nm, but were otherwise similar to those obtained at 450 °C.

For analysis of the phase development during heating gel powders prepared in air from the same precursor solutions as the films were studied with a combination of TG-DTA, XRD and IR spectroscopy. The gel powders contained a large amount of water and hydroxo groups with no remaining organics and can be described as Fe(III)-oxo-hydroxides. The water was removed before 130 °C, and only minute amounts of hydroxyl groups remained at 280 °C, which were removed before 400 °C. No differences were observed when Ti was incorporated in the gel.

Figure 14 shows soft X-ray absorption measurements, as above in sections 5.1, 5.2, and 5.3. Remarkably, here again we observe the same modifications to X-ray absorption spectra induced by Ti incorporation. The O *K*-edge shows a low-lying band of unoccupied O 2p states hybridized with Fe 3d states. No discernible changes to the Fe *L*_{2,3}-edge spectra are observed as a result of Ti incorporation.

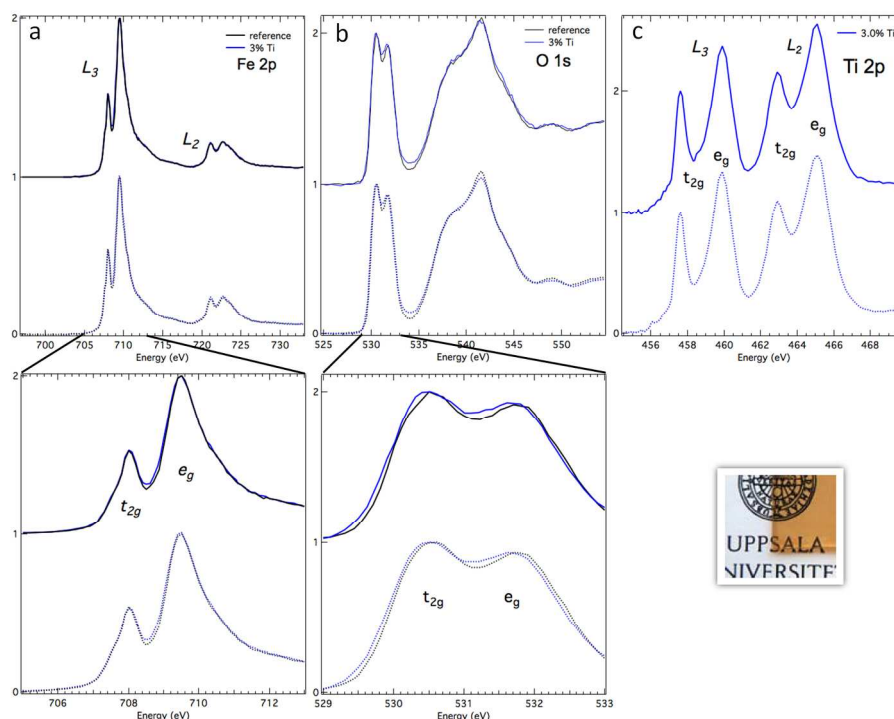


Figure 14. Soft X-ray absorption spectra of α -Fe₂O₃ and Ti: α -Fe₂O₃ thin films fabricated by an all-alkoxide sol-gel route. (a) Fe *L*_{2,3}-edge XAS full spectral range (top) and expanded view of *L*₃ band (bottom). (b) O *K*-edge XAS full spectral range (top) and expanded view of the O 2p - Fe 3d hybridized region in α -Fe₂O₃. (c) Ti *L*_{2,3}-edge XAS full spectral range. This panel also includes a reference spectrum for anatase TiO₂. In all panels, the total electron yield is represented by solid lines and the total fluorescence yield by dashed lines.

5.5 Nanostructured arrays fabricated by aqueous chemical growth

Next, we present select measurements on Ti: α -Fe₂O₃ fabricated by aqueous chemical growth, using methods described in Ref ⁹⁶. To produce the Ti-modified samples, the methodology was modified slightly to include a Ti precursor, as described in the Experimental section. Figure 15a and b show the influence of Ti precursor on the morphology of resultant films. It is clear there is a strong influence; the α -Fe₂O₃ has a

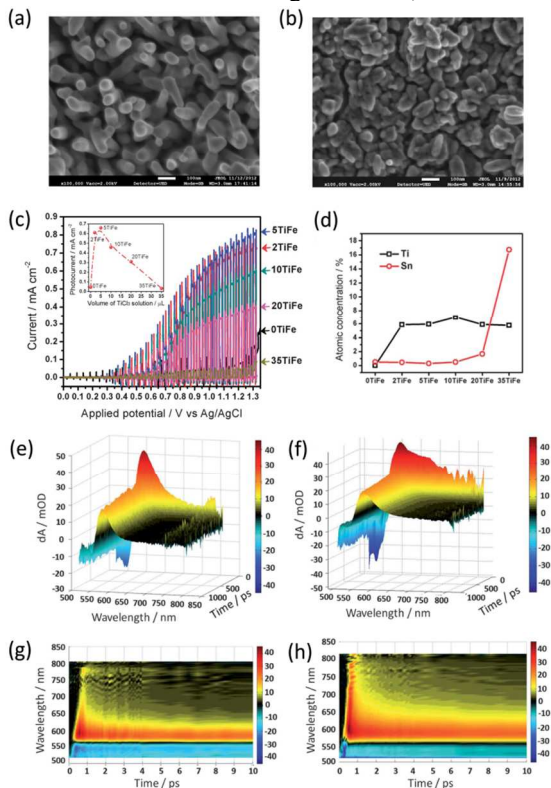


Figure 15. SEM images and soft X-ray absorption spectra of Ti: α -Fe₂O₃ nanostructured films fabricated by aqueous chemical growth. (a) SEM image of α -Fe₂O₃ annealed at 750 °C. (b) SEM image of Ti: α -Fe₂O₃ annealed at 750 °C. (c) Light-chopped current–potential plots for α -Fe₂O₃ and Ti: α -Fe₂O₃ films under simulated solar light (AM 1.5G, 100 mW cm⁻²). The inset shows the photocurrent at 1.0 V vs. Ag/AgCl plotted as a function of the volume of TiCl₃ in the precursor solution. (d) Surface concentrations of Ti and Sn in samples based on XPS analysis. Three-dimensional spectral evolution of the transient difference absorption profiles for (e) no TiCl₃ and (f) 5 μ L TiCl₃ in precursor solution. Two-dimensional top-down views of the transient difference absorption profiles for (g) α -Fe₂O₃ and (h) Ti: α -Fe₂O₃ (5 μ L TiCl₃ in precursor solution) 0–10 ps windows. From Ref 58.

To understand the mechanism by which Ti incorporation improves photoelectrochemical performance, ultrafast transient absorption spectroscopy measurements were performed. This technique facilitates evaluation of the lifetime of excited carriers on ultrafast time scales. It therefore can provide information on the recombination dynamics of electrons and holes, knowledge of which is a critical aspect of photoelectrode design. Figures 15e–h show three- (e,f) and two-dimensional (g,h) spectral evolutions of the transient difference absorption profiles for unmodified (e,g) and Ti: α -Fe₂O₃ (f,h) films. The change in optical density upon excitation is presented with respect to probe wavelength and time. The data, discussed in detail in Ref 58, show that there is no significant change in electron-hole recombination dynamics up to 1000 ps when Ti is incorporated

rod structure⁹⁰ that is modified by the high temperature annealing process and the Ti: α -Fe₂O₃ is better characterized as a porous or nanostructured film. Figure 15c shows the strong influence of Ti precursor concentration on photocurrent density, data which was originally reported in Ref 58. There is an optimum photocurrent value for the sample fabricated with 5- μ L TiCl₃ in the precursor solution, which according to the surface concentration plot in Figure 15d corresponds to about 6 at.% Ti.

during hydrothermal growth. On longer time scales however, there is some increase in carrier lifetime, which may suggest a change in carrier dynamics. This observation warrants further investigation.⁵⁸

Ti $L_{2,3}$ -edge X-ray absorption measurements on the sample fabricated with 20- μ L TiCl₃ in the precursor solution, after post-annealing at 650 and 750 °C, are shown in Figure 16. The characteristics of the Ti L -edge XAS data is discussed in more detail below for this system.

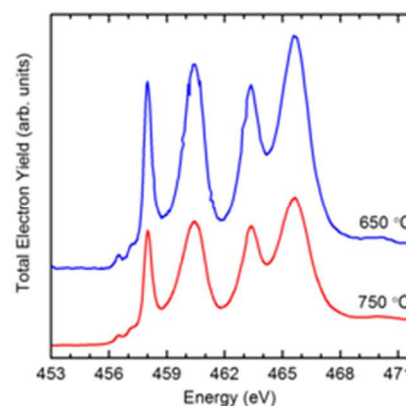


Figure 16. Ti $L_{2,3}$ -edge absorption spectra of Ti: α -Fe₂O₃ nanostructured films fabricated by aqueous chemical growth.

5.6 Discussion

5.6.1 Fe $L_{2,3}$ -edge XAS

In Figures 8, 10, 12, and 14 above, the panels in (a) show the Fe $L_{2,3}$ -edge X-ray absorption spectra of α -Fe₂O₃ and Ti: α -Fe₂O₃ photoelectrodes. This absorption channel probes the Fe 2p-to-3d transitions and provides a signature of the Fe oxidation state. Here, the line shapes of the $L_{2,3}$ -edge absorption spectra for all samples are dominated by the Fe³⁺ multiplet structure.⁹⁷ The shape of the L_3 absorption band (707–715 eV) results primarily from absorption into states influenced by Fe³⁺ ions in the O_h sites of the corundum structure.

Irrespective of the synthesis technique, in the Fe L_3 absorption band we observe that Ti incorporation is associated with a reduction in the intensity of the first peak with respect to the intensity of the second. We previously observed this relationship in the Fe L_3 band peak intensity in a study on the interface between α -Fe₂O₃ and SnO₂:F.⁹⁸ Prior to this, the intensity of the first peak had been assigned to reflect the density of electronic states corresponding to O_h -site occupation of Fe³⁺ ions,⁹⁹ as well as to changes in iron-oxygen distances.⁹⁷ It is possible therefore that the origin of the first peak intensity

reduction is related to the influence of titanium on distorting the structure and O_h symmetry of the system.

5.6.2 O K -edge XAS

The intensity within the structure of the Fe 3d band of the O K -edge absorption spectrum (between about 529 and 534 eV) shows distinct variation from that of α -Fe₂O₃ with the inclusion of Ti for all synthesis techniques. This band of the absorption spectrum is arguably the most important for the present discussion. In the soft X-ray absorption process, a core electron is excited through an electric dipole transition to a near-threshold state. The spectra generated yield information relating to the symmetry-projected partial density-of-states of the excited state. Therefore, the O K -edge absorption spectrum provides a representation of the O 2p unoccupied density-of-states by excitation of core O 1s electrons. Through the hybridization of metal states with O 2p states, we observe states most relevant to electron conduction in the oxide photoanodes.

In Ti: α -Fe₂O₃ we expect the conduction band minimum to be strongly modified by Ti s and d orbital character. The presence of Ti s and d states near the conduction band minimum is consistently predicted by calculations on the Ti: α -Fe₂O₃ system,⁷⁶ and is shown in Figure 4.⁶⁸ Mixing of Ti s and d orbitals near the lowest unoccupied states of α -Fe₂O₃ likely influences the efficiency of electron conduction in operating PEC electrodes. These bands are more dispersive than Fe d bands, and in the band structure picture would tend to reduce the effective mass of electrons.⁶⁸

It is somewhat surprising that no energetic shifts in the conduction band minima were observed to be associated with Ti incorporation, within the resolution of our measurements. Bandgap reduction has been predicted to occur with Ti doping; in Ref 59 for example, the impurity is associated with a computed band gap reduction of ~0.2 to 0.3 eV relative to pure α -Fe₂O₃, due to the appearance of empty Ti 3d states below and overlapping the conduction band minimum.

5.6.3 Ti $L_{2,3}$ -edge XAS

In Figures 8, 10, 12, and 14 above, the panels in (c), as well as Figure 16, show the Ti $L_{2,3}$ -edge X-ray absorption spectra of the α -Fe₂O₃ and Ti: α -Fe₂O₃ photoelectrodes. As at the Fe L -edge, this representation of Ti 2p - to - 3d transitions is closely related to the multiplet structure of the Ti cation. Here, for all synthesis techniques, the spectral line shapes originate from Ti⁴⁺.

It has previously been suggested that tetravalent Ti could be incorporated into α -Fe₂O₃ photoelectrodes as the rutile polymorph of TiO₂.¹⁰⁰ This model is attractive in that it avoids face sharing of TiO₆ and FeO₆ octahedra, which is a highly unstable configuration due to the associated high cation repulsions.¹⁰¹ $L_{2,3}$ -edge XAS can be used to probe the long-range order around the Ti site, through transitions into e_g orbitals, which point in the direction of and strongly hybridize with oxygen ligands. The line shape of the L_{3-e_g} band (centered at 460 eV) is known to provide a fingerprint of the TiO₂ polymorph.¹⁰² For titania compounds, the L_{3-e_g} band possesses an asymmetric doublet, which can be reproduced in simulations by inclusion of large atom clusters (on the order of 1 nm of material).¹⁰³ The doublet structure is absent in disordered titania

aerogels¹⁰² and at the interface between TiO₂ and fluorine-doped tin dioxide, confirming its origin from long-range order.¹⁰⁴ Here, for all synthesis methods, the line shapes of the L_{3-e_g} bands (near 463 eV) for Ti: α -Fe₂O₃ and in particular the absence of any characteristic doublet structure suggests a lack of long-range order around Ti⁴⁺. This result is consistent with Fe and Ti K -edge absorption spectroscopy measurements on MBE-grown Ti-doped α -Fe₂O₃, which show no presence of anatase or rutile TiO₂.²⁴

5.6.4. Effect of orientation and surface and grain morphology

The X-ray absorption spectra in Figures 8, 10, 12, and 14 show an important difference when measured in total electron yield and total fluorescence yield. The probe depth of total electron yield is on the order of a few nanometers, due to the short inelastic mean free path of electrons in oxides. Total fluorescence yield, on the other hand, probes a physical distance on the order of one hundred nanometers due to the comparatively longer path length of X-rays in the solid. The difference in probe depth is clearly reflected for the case of the ALD sample that is 36 nm thick. Total electron yield spectra for the O K -edge (Figure 10b, top) show only the characteristic spectrum for α -Fe₂O₃, whereas total fluorescence yield spectra (Figure 10b, bottom) show spectra that are in fact a composite of α -Fe₂O₃ and SnO₂:F, the transparent conductive oxide substrate. The peak near 534 eV originates from Sn 5s - O 2p hybridized states in SnO₂.¹⁰⁴

Comparison of these spectra for a given sample reveals that the features associated with Ti incorporation, especially those at the O K -edge, are more dramatic for total electron yield. This suggests that the electronic structure is modified more dramatically near the surface region, since the integrated volume that is sampled is smaller and closer to the surface for total electron yield.

The observation that electronic structure modifications due to Ti incorporation are weighted more heavily near the surface is significant for this material system. A recent perspective article from Sivula¹⁰⁵ highlights the significance of surface states for the high efficiency of α -Fe₂O₃-based photoanodes for water oxidation. The overpotential required for water oxidation using valence band holes is currently prohibitively high for solar fuel synthesis devices. The distribution of surface electronic states and their occupancy appears to be determinative for overpotential losses when water oxidized directly on the surface of α -Fe₂O₃ electrodes. That the electronic structure modifications due to Ti incorporation are observed here to be more concentrated at the surface is highly relevant to this discussion. Notably, in a recent analysis of the structural and electrical properties of sintered Ti: α -Fe₂O₃, Nikolic *et al.*¹⁰⁶ identified a dominant grain boundary contribution to electron conduction. Through analysis of neutron diffraction measurements, Curry *et al.*¹⁰⁷ noted that there is an essential difference between the magnetic properties of sintered and single crystalline Ti: α -Fe₂O₃, leading to a suggestion that impurities in the sintered materials exist at grain boundaries.

On a related topic, the thin film textures observed in the literature for Ti: α -Fe₂O₃ (shown in Table 1), as well as the

morphologies presented in the SEM images of this study, show that the incorporation of Ti strongly influences growth dynamics of α -Fe₂O₃ crystals. This is particularly clear for the films grown by PLD, whose morphologies are shown in Figure 7, and the films fabricated by aqueous chemical growth, shown in Figure 15. In addition to the electronic structure correlates to efficiency enhancement shown above, here we provide a short note on the possible role of titanium-influenced grain structure on photoelectrochemical performance.

The film morphology variation can be understood in terms of thermodynamic principles: the shape, size, and orientation of crystallites depends on the surface tension (or surface energy per unit volume) of the structure during growth.¹³ Although a detailed model for crystal growth is not possible here, one can predict that Ti is involved in the grain growth process through the minimization of surface energy, associated with the surface area and properties of grain boundaries and exposed crystal faces. Surface energy per unit area depends on chemical composition, atomic reconstruction, crystallographic orientation, and atomic scale roughness.⁸⁹ Diffusion of charged Ti species to grain boundaries influences grain structure and morphology by altering the physical properties of crystal faces and interfaces, and therefore the configuration associated with the lowest free energy. This is especially true for α -Fe₂O₃ crystals, which are highly polarized.

It is also possible that Ti⁴⁺ segregates at grain boundaries and suppresses electron-hole recombination by passivation of dangling bonds, or by quenching growth of interfacial sub-oxide phases. This is consistent with observations made in Ref 27, namely that conductivity enhancements alone are insufficient to explain the strong effect of Ti doping on performance.

It has been observed in structural characterization of magnetron-sputtered films²⁶ that α -Fe₂O₃ tends to grow [110] textured; that is, the [110] crystallographic direction is oriented perpendicular to the substrate surface. When Ti is incorporated, the texture of the thin films tends to move away from the [110] direction. For the PLD-synthesized films presented here, a slight texturing away from [110] is also observed by X-ray diffraction (data not shown) through corresponding attenuation of the [110] diffraction peak.

It is interesting that PEC performance improves with Ti incorporation despite the tendency for the films to grow oriented away from the [110] axis, a direction of high conductivity in α -Fe₂O₃. As discussed above, the conductivity within *a-b* planes, to which [110] is parallel, is orders of magnitude higher than in the orthogonal direction [001]. As discussed above, many groups suggest that Ti incorporation enhances the efficiency of majority carrier (electron) collection at the back contact. In this context, the results seem to suggest that the conductivity enhancement associated with Ti impurities in the direction normal to the substrate surface (and/or any associated improved electron collection at the back contact interface) is large enough to counteract any negative impact associated with texturing in lower-conductivity crystallographic direction.

6. Conclusions

In summary, the role of titanium impurities in the improved photoelectrochemical performance of hematite photoanodes has

been discussed. Synchrotron-based soft X-ray absorption spectroscopy measurements were performed on sets of electrodes fabricated by five independent physical and chemical techniques. The effect of titanium impurities on the electronic structure is reflected in several spectral characteristics. Absorption spectra at the oxygen *K*-edge show that irrespective of synthesis technique, Ti incorporation is associated with new oxygen 2p-hybridized states, overlapping with and distorting the known unoccupied Fe 3d-O 2p band of α -Fe₂O₃. This is likely an indication of mixing of Ti s and d states in the conduction band of α -Fe₂O₃. Contrasting spectra from electron yields and fluorescent X-rays shows the effects of Ti incorporation on the conduction band are more pronounced in the near-surface region. Titanium *L*_{2,3}-edge absorption spectra show titanium is incorporated into α -Fe₂O₃ as Ti⁴⁺ by both fabrication methods, with no long-range titania order detected. Fe *L*_{2,3}-edge absorption spectra indicate that Ti incorporation is not associated with the formation of any significant concentrations of Fe²⁺.

Based on these observations, the next steps toward a continuing understanding of hematite photoelectrode efficiency enhancement driven by Ti incorporation should be comprehensive evaluation of magnetic structure¹⁰⁸ and crystal growth mechanisms. It is likely that both of these features will be critical to developing a complete understanding of optimal electrode properties. In particular, understanding the role of the surface in Ti-modified electrodes should be emphasized in future work. Given the various explanations for the conductivity and PEC performance enhancement associated with Ti doping, such studies should be conducted on materials fabricated in the same conditions known to effect appreciable changes in photocurrent. Novel *in situ* electrical conductivity measurements provide important new insights toward our developing understanding of such systems.^{109,110} Finally, multiple time-scale studies of carrier dynamics by laser transient spectroscopy and/or time-resolved X-ray spectroscopy¹¹¹ will also provide additional fundamental understanding (e.g. time scale and chemical nature of recombination sites, small polaron formation) crucial for performance and efficiency optimization.

7. Experimental section

Soft X-ray absorption spectroscopy

Soft X-ray absorption spectroscopy measurements were conducted at Beamline 8.0.1 of the Advanced Light Source (ALS) at Lawrence Berkeley National Laboratory. The energy resolution was set to 0.2-0.3 eV at all investigated edges (O *K*, Fe *L*_{2,3}, Ti *L*_{2,3}). The photon energy was calibrated using the first peak of the O 1s absorption spectrum of TiO₂ rutile powder (531.8 eV) for the O *K*-edge, the first peak of the Ti 2p absorption spectrum of TiO₂ rutile powder (458.0 eV) for the Ti *L*-edges, and the main *L*₃ peak of the Fe 2p absorption spectrum of reference α -Fe₂O₃ (709.5 eV) for the Fe *L*-edges. Total electron yield (TEY) and total fluorescence yield (TFY) data were collected simultaneously. For TFY, a channel plate detector with an Al filter was used. In all cases, the absorption spectra were normalized to the incident photon flux by dividing the XAS intensities by the current from a gold-coated mesh located in the x-ray beam path close to the sample position. All spectra shown were interpolated with a cubic spline function.

The low-energy, pre-edge background was subtracted by a linear fit.

Pulsed laser deposition

Thin films were fabricated by deposition of species from pulsed laser ablation of rotating pressed polycrystalline targets in an O₂ ambient (reactive pulsed laser deposition) using a Lambda Physik LPX 200 KrF Excimer Laser (248 nm). Films were deposited onto SnO₂:F-coated glass (FTO; Pilkington TEC7). The target compositions were α -Fe₂O₃, α -Fe₂O₃ (1 wt % TiO₂), and α -Fe₂O₃ (2.5 wt % TiO₂). A stainless steel chamber was evacuated to a base pressure of about 10⁻⁴ Torr, after which O₂ gas (industrial grade) was flowed through the evacuated chamber for 30 minutes at 18 sccm, as set by a mass flow controller, to replace residual gases. The FTO substrate was mounted to a substrate holder using conductive Ag paste. Deposition occurred at a laser fluence of ~ 1 J cm⁻² per pulse with pulse frequency of 9 Hz for 4 hrs. The O₂ pressure during deposition was approximately 4×10⁻³ Torr as measured by a pirani gauge. Before deposition the target was ablated for several minutes at the deposition laser parameters to remove any contaminants from the target surface, during which the entire substrate was masked with a mechanical shutter. Throughout deposition the sample was maintained at 300 °C using a resistance heater and thermocouple embedded in the substrate holder. After deposition the chamber was sealed and the sample was allowed to cool to room temperature in the quiescent low-pressure O₂ ambient.

Scanning electron microscopy (SEM) images in Figure 7 were obtained with a Hitachi environmental field emission scanning electron microscope (Model S-4300SE/N) with an accelerating voltage of 3-5 kV, operating in secondary electron detection mode. Energy dispersive X-ray spectrometry (EDS) measurements were performed in the SEM at 15 kV. Spectral transmittance measurements were taken on the α -Fe₂O₃/FTO/glass samples with a Perkin Elmer Lambda Spectrophotometer fitted with an integrating sphere over the wavelength range 300 to 800 nm at a wavelength interval of 2 nm. The samples were illuminated at the α -Fe₂O₃ surfaces. For the photoelectrochemical measurements the electrolyte was prepared with 18.1 MΩ-cm water with 1 M NaOH. The measurements were conducted using standard techniques, as described in Ref 87.

Atomic layer deposition

Thin films of Ti:α-Fe₂O₃ were deposited on (FTO)-coated glass substrates (Hartford Glass) by atomic layer deposition (Savannah 100, Cambridge Nanotech Inc.) using a procedure described in Ref 11.

Sol-flame synthesis

Ti:α-Fe₂O₃ nanostructures were fabricated by the sol-flame technique.¹² First, arrays of α-Fe₂O₃ nanorods (NRs) with an average length about 350 nm was synthesized on FTO (TEC-8, Pilkington) substrates by air-annealing (550 °C) of hydrothermally grown FeOOH NRs.⁹⁶ Then, the α-Fe₂O₃ NRs were dip-coated with a Ti-precursor solution (10mM TTIP in IPA) and finally annealed in a 1000 °C flame for 5 min to enable rapid thermal diffusion of Ti. Two different TiO₂ precursor

solutions were used (0.01 M and 0.05 M titanium-tetraisopropoxide in isopropyl alcohol) to vary the doping concentration.

Aqueous chemical growth

Ti:α-Fe₂O₃ nanostructures were fabricated using an aqueous chemical synthesis methodology described previously.⁹⁶ The precursor solution was modified to contain 20 wt% titanium trichloride (TiCl₃).

Sol-gel synthesis

Ti:α-Fe₂O₃ films with 0 and 3 metal atom % Ti were fabricated by the sol-gel technique using 0.3 M (metal) toluene - methoxy-ethanol solutions with Fe(III)-methoxy-ethoxide and Ti(OPrⁱ)₄ as precursors. Films were deposited by spin-coating at 3000 rpm on a variety of substrates including; Si/SiO₂, Si/SiO₂/Pt, α-Al₂O₃ (0001) and FTO. The obtained gel films were heated in air to 450 °C at 20 °C min⁻¹ to yield α-Fe₂O₃ films. The Grazing Incidence (1°) X-ray diffractograms were obtained with a Siemens D5000 instrument. The SEM images were obtained with a FEI Merlin instrument and the TEM images of pieces of film scraped off the substrate were studied with a JEOL 2100F TEM, equipped with an EDS unit. The TG-DTA curves and IR spectra of gels and samples heated to 130, 280, 400 and 450 °C were made with a Netsch STA 409 Pc Luxx instrument and the IR spectra with a Perkin-Elmer Spectrum One instrument equipped with a diamond ATR (Pike GladiATR) unit. All handling of the alkoxides was carried out in an Ar filled glove-box. The titanium tetraisopropoxide (Ti(OPrⁱ)₄) (Aldrich 97%) was used as received after the accurate Ti concentration had been measured gravimetrically and the Fe(III) methoxy-ethoxide was synthesised by metathesis. The alkoxides and solvents were purified and treated following a procedure given elsewhere.¹¹²

Acknowledgements

C.X.K. and B.E.K. acknowledge support from the Grand Challenges Program at Princeton University. E.A.C. acknowledges the U.S. Department of Energy, Office of Basic Energy Sciences. NSF/CMMI under grant #1036076; by the U.S. Department of Energy, Office of Energy Efficiency and Renewable Energy; and by the Office of Basic Energy Sciences under the Contracts DE-SC0006931, DE-AC02-05CH11231 (ALS), DE-FG02-01ER45917 (end station). T.W.H. thanks the National Science Foundation (CHE-1150378) for support. G.W. thanks the Swedish Science Council (VR) for their support. S. S. and L.V. thank the International Research Center for Renewable Energy, State Key Laboratory of Multiphase Flow in Power Engineering, Xian Jiaotong University, the Thousand Talents plan and the National Natural Science Foundation of China (No. 51121092 and 51102194).

References

- [1] Y. Tachibana, L. Vayssieres and J. R. Durrant, *Nature Photon.*, 2012, **6**, 511-518.
- [2] J. Y. Kim, G. Magesh, D. H. Youn, J.-W. Jang, J. Kubota, K. Domen and J. Sung Lee, *Sci. Rep.*, 2013, **3**, 2681.
- [3] L. Vayssieres, C. Sathe, S. M. Butorin, D. K. Shuh, J. Nordgren and J.-H. Guo, *Adv. Mater.*, 2005, **17**, 2320-2323.

- [4] D. K. Bora, A. Braun and E. C. Constable, *Energy Environ. Sci.*, 2013, **6**, 407-425.
- [5] F. E. Osterloh, *Chem. Soc. Rev.*, 2013, **42**, 2294-2320.
- [6] T. Hisatomi, J. Kubota and K. Domen, *Chem. Soc. Rev.*, 2014, Advance Article, DOI:10.1039/C3CS60378D
- [7] G. Wang, Y. Ling, H. Wang, L. Xihong and Y. Li, *J. Photochem. Photobiol C: Photochem. Rev.*, 2014, **19**, 35-51.
- [8] H. Dotan, O. Kfir, E. Sharlin, O. Blank, M. Gross, I. Dumchin, G. Ankonina and A. Rothschild, *Nature Mater.*, 2013, **12**, 158-164.
- [9] P. S. Bassi, Gurudayal, L. H. Wong and J. Barber, *Phys. Chem. Chem. Phys.*, 2014, **16**, 11834-11842.
- [10] D. H. Lowndes, D. B. Geohegan, A. A. Puzos, D. P. Norton and C. M. Rouleau, *Science*, 1996, **273**, 898-903.
- [11] O. Zandi, B. M. Klahr and T. W. Hamann, *Energy Environ. Sci.*, 2013, **6**, 634-642.
- [12] I. S. Cho, C. H. Lee, Y. Feng, M. Logar, P. M. Rao, L. Cai, D. R. Kim, R. Sinclair and X. L. Zheng, *Nature Comm.*, 2013, **4**, 1723.
- [13] L. Vayssieres, *Int. J. Nanotechnol.*, 2004, **1**, 1-42.
- [14] E. L. Miller, R. E. Rocheleau and X. M. Deng, *Int. J. Hydrogen Energy*, 2003, **28**, 615-623.
- [15] J. Brilliet, J.-H. Yum, M. Cornuz, T. Hisatomi, R. Solarska, J. Augustynski, M. Grätzel and K. Sivula, *Nature Photon.*, 2012, **6**, 824-828.
- [16] K. S. Joya, Y. F. Joya, K. Ocaoglu and R. van de Krol, *Angew. Chem. Int. Ed.*, 2013, **52**, 10426-10437.
- [17] D. A. Wheeler, G. Wang, Y. Ling, Y. Li and J. Z. Zhang, *Energy Environ. Sci.*, 2012, **5**, 6682-6702.
- [18] I. S. Cho, Z. Chen, A. J. Forman, D. R. Kim, P. M. Rao, T. F. Jaramillo and X. Zheng, *Nano Lett.*, 2011, **11**, 4978-4984.
- [19] C. Santato, M. Ulmann and J. Augustynski, *Adv. Mater.*, 2001, **13**, 511-514.
- [20] A. Kleiman-Shwarsstein, M. N. Huda, A. Walsh, Y. Yan, G. D. Stucky, Y.-S. Hu, M. M. Al-Jassim and E. W. McFarland, *Chem. Mater.*, 2010, **22**, 510-517.
- [21] F. J. Morin, *Phys. Rev.*, 1951, **83**, 1005-1010.
- [22] N. T. Hahn and C. B. Mullins, *Chem. Mater.*, 2010, **22**, 6474-6482.
- [23] S. R. Pendlebury, A. J. Cowan, M. Barroso, K. Sivula, J. Ye, M. Grätzel, D. R. Klug, J. Tang and J. R. Durrant, *Energy Environ. Sci.*, 2012, **5**, 6304-6312.
- [24] B. Zhao, T. C. Kaspar, T. C. Droubay, J. McCloy, M. E. Bowden, V. Shutthanandan, S. M. Heald and S. A. Chambers, *Phys. Rev. B*, 2011, **84**, 245325.
- [25] R. Shinar and J. H. Kennedy, *Solar Energy Mater.*, 1982, **6**, 323-335.
- [26] H. Tang, M. A. Martin, H. Wang, T. Deutsch, M. Al-Jassim, J. Turner and Y. Yan, *J. Appl. Phys.*, 2011, **110**, 123511.
- [27] J. A. Glasscock, P. R. F. Barnes, I. C. Plumb and N. Savvides, *J. Phys. Chem. C*, 2007, **111**, 16477-16488.
- [28] C. X. Kronawitter, S. S. Mao and B. R. Antoun, *Appl. Phys. Lett.*, 2011, **98**, 092108.
- [29] M. H. Lee, J. H. Park, H. S. Han, H. J. Song, I. S. Cho, J. H. Noh and K. S. Hong, *Int. J. Hydrogen Energy*, 2013, Article in Press, <http://dx.doi.org/10.1016/j.ijhydene.2013.10.031>
- [30] X. Li, N. C. Fan and H. J. Fan, *Chem. Vap. Deposition*, 2013, **19**, 104-110.
- [31] S. A. Chambers, *J. Phys-Condens. Matter*, 2008, **20**, 264004.
- [32] C. Y. Kim, *Thin Solid Films*, 2011, **519**, 5996-5999.
- [33] H. Magnan, D. Stanescu, M. Rioult, E. Fonda and A. Barbier, *Appl. Phys. Lett.*, 2012, **101**, 133908.
- [34] A. A. Tahir, K. G. U. Wijayantha, S. Saremi-Yarahmadi, M. Mazhar and V. McKee, *Chem. Mater.*, 2009, **21**, 3763-3772.
- [35] A. Kay, I. Cesar and M. Grätzel, *J. Am. Chem. Soc.*, 2006, **128**, 15714-15721.
- [36] M. Rahman, N. Wadnerkar, N. J. English and J. M. D. MacElroy, *Chem. Phys. Lett.*, 2013, **592**, 242-246.
- [37] P. Zhang, A. K. Shwarsstein, Y. S. Hu, J. Lefton, S. Sharma, A. J. Formand and E. W. McFarland, *Energy Environ. Sci.*, 2011, **4**, 1020-1028.
- [38] H. Tang, W.-J. Yin, M. A. Matin, H. Wang, T. Deutsch, M. M. Al-Jassim, J. A. Turner and Y. Yan, *J. Appl. Phys.*, 2012, **111**, 073502.
- [39] J. H. He and B. A. Parkinson, *ACS Comb. Sci.*, 2011, **13**, 399-404.
- [40] R. Franking, L. Li, M. A. Lukowski, F. Meng, Y. Tan, R. J. Hamers and S. Jin, *Energy Environ. Sci.*, 2013, **6**, 500-512.
- [41] L. Wang, C.-Y. Lee and P. Schmuki, *Electrochem. Comm.*, 2013, **30**, 21-25.
- [42] Y.-S. Hu, A. Kleiman-Shwarsstein, G. D. Stucky and E. W. McFarland, *Chem. Comm.*, 2009, 2652-2654.
- [43] S. Kumari, A. P. Singh, Sonal, D. Deva, R. Shrivastav, S. Dass and V. R. Satsangi, *Int. J. Hydrogen Energy*, 2010, **35**, 3985-3990.
- [44] C. J. Sartoretti, B. D. Alexander, R. Solarska, I. A. Rutkowska, J. Augustynski and R. Cerny, *J. Phys. Chem. B*, 2005, **109**, 13685-13692.
- [45] M. Zhang, W. Luo, Z. Li, T. Yu and Z. Zou, *Appl. Phys. Lett.*, 2010, **97**, 042105.
- [46] X. Lian, X. Yang, S. Liu, Y. Xu, C. Jiang, J. Chen and R. Wang, *Appl. Surf. Sci.*, 2012, **258**, 2307-2311.
- [47] G. Wang, Y. Ling, D. A. Wheeler, K. E. N. George, K. Horsley, C. Heske, J.Z. Zhang and Y. Li, *Nano Lett.*, 2011, **11**, 3503-3509.
- [48] P. Shangguan, S. Tong, H. Li and W. Leng, *RSC Adv.*, 2013, **3**, 10163-10167.
- [49] J. Deng, J. Zhong, A. Pu, D. Zhang, M. Li, X. Sun and S.-T. Lee, *J. Appl. Phys.*, 2012, **112**, 084312.
- [50] D. Cao, W. Luo, M. Li, J. Feng, Z. Li and Z. Zou, *CrystEngComm*, 2013, **15**, 2386-2391.
- [51] Z. Fu, T. Jiang, Z. Liu, D. Wang, L. Wang and T. Xie, *Electrochem. Acta*, 2014, In Press. <http://dx.doi.org/10.1016/j.electacta.2014.02.132>
- [52] C. Miao, S. Ji, G. Xu, G. Liu, L. Zhang and C. Ye, *ACS Appl. Mater. Interfaces*, 2012, **4**, 4428-4433.
- [53] C. Miao, T. Shi, G. Xu, S. Ji and C. Ye, *ACS Appl. Mater. Interfaces*, 2013, **5**, 1310-1316.
- [54] B. A. Balko and K. M. Clarkson, *J. Electrochem. Soc.* 2001, **148**, E85-E91.
- [55] T.-Y. Yang, H.-Y. Kang, K. Jin, S. Park, J.-H. Lee, U. Sim, H.-Y. Jeong, Y.-C. Joo and K. T. Nam, *J. Mater. Chem. A*, 2014, **2**, 2297-2305.
- [56] D. Cao, W. Luo, J. Feng, X. Zhao, Z. Lia and Z. Zou, *Energy Environ. Sci.*, 2014, **7**, 752-759.
- [57] A. Pu, J. Deng, M. Li, J. Gao, H. Zhang, Y. Hao, J. Zhong and X. Sun, *J. Mater. Chem. A*, 2013, **2**, 2491-2497.
- [58] S. Shen, C. X. Kronawitter, D. A. Wheeler, P. Guo, S. A. Lindley, J. Jiang, J. Z. Zhang, L. Guo and S. S. Mao, *J. Mater. Chem. A*, 2013, **1**, 14498-14506.
- [59] T. Droubay, K. M. Rosso, S. M. Heald, D. E. McCready, C. M. Wang and S. A. Chambers, *Phys. Rev. B*, 2007, **75**, 104412.
- [60] M. Rioult, H. Magnan, D. Stanescu and A. Barbier, *J. Phys. Chem. C* 2014, **118**, 3007-3014.

- [61] E. Thimsen, S. Biswas, C. S. Lo and P. Biswas, *J. Phys. Chem. C* 2009, **113**, 2014-2021.
- [62] J. Baltrusaitis, Y.-S. Hu, E. W. McFarland and A. Hellman, *ChemSusChem*, 2013, **7**, 162-171.
- [63] X. Y. Meng, G. W. Qin, S. Li, X. H. Wen, Y. P. Ren, W. L. Pei and L. Zuo, *Appl. Phys. Lett.*, 2011, **98**, 112104.
- [64] A. J. Cohen, P. Mori-Sanchez and W. Yang, *Science*, 2008, **321**, 792-794.
- [65] V. I. Anisimov, J. Zaanen and O. K. Andersen, *Phys. Rev. B*, 1991, **44**, 943-954.
- [66] A. Bandyopadhyay, J. Velev, W. H. Butler, S. K. Sarker and O. Bengone, *Phys. Rev. B*, 2004, **69**, 174429.
- [67] J. Velev, A. Bandyopadhyay, W. H. Butler, and S. Sarker, *Phys. Rev. B*, 2005, **71**, 205208
- [68] M. N. Huda, A. Walsh, Y. Yan, S.-H. Wei and M. M. Al-Jassim, *J. Appl. Phys.*, 2010, **107**, 123712.
- [69] P. Liao, J. A. Keith and E. A. Carter, *J. Am. Chem. Soc.*, 2012, **134**, 13296-13309.
- [70] P. Liao, M. C. Toroker and E. A. Carter, *Nano Lett.*, 2011, **11**, 1775-1781.
- [71] K. M. Rosso, D. M. A. Smith and M. Dupuis, *J. Chem. Phys.*, 2003, **118**, 6455.
- [72] N. Iordanova, M. Dupuis and K. M. Rosso, *J. Chem. Phys.* 2005, **122**, 144305.
- [73] P. Robinson, R. J. Harrison, S. A. McEnroe and R. B. Hargraves, *Am. Mineral*, 2004, **89**, 725-747.
- [74] W. H. Butler, A. Bandyopadhyay and R. Srinivasan, *J. Appl. Phys.*, 2003, **93**, 7882.
- [75] A. Celik-Aktas, T. Droubay, S. A. Chambers and M. Gajdardziska-Josifovska, *Microsc. Microanal.*, 2007, **13**, 820-821.
- [76] R. Rivera and A. Stashans, *Sol. State Sci.*, 2010, **12**, 1409-1412.
- [77] S. Gota, M. Gautier-Soyer and M. Sacchi, *Phys. Rev. B*, 2001, **64**, 224407.
- [78] R. D. Zysler, D. Fiorani and A. M. Testa, *J. Magn. Magn. Mater.*, 2001, **224**, 5-11.
- [79] V. Zelenak, A. Zelenakova, J. Kovac, U. Vainio and N. Murafa, *J. Phys. Chem. C*, 2009, **113**, 13045-13050.
- [80] J. Jacob and M. A. Khadar, *J. Magn. Magn. Mater.*, 2010, **322**, 614-621.
- [81] I. R. Macdonald, R. F. Howe, S. Saremi-Yarahmadi and K. G. U. Wijayantha, *J. Phys. Chem. Lett.*, 2010, **1**, 2488-2492.
- [82] C. X. Kronawitter, I. Zegkinoglou, S. Shen, J. Guo, F. J. Himpsel, S. S. Mao and L. Vayssieres, *Phys. Chem. Chem. Phys.*, 2013, **15**, 13483-13488.
- [83] F. M. F. de Groot, M. Grioni, J. C. Fuggle, J. Ghijsen, G. A. Sawatzky and H. Petersen, *Phys. Rev. B*, 1989, **40**, 5715.
- [84] C. X. Kronawitter, J. R. Bakke, D. A. Wheeler, W.-C. Wang, C. Chang, B. R. Antoun, J. Z. Zhang, J. Guo, S. F. Bent, S. S. Mao and L. Vayssieres, *Nano Lett.*, 2011, **11**, 3855-3861.
- [85] F. M. F. de Groot, *Chem. Rev.*, 2001, **101**, 1779-1808.
- [86] G. Korotcenkov, *Mater. Sci. Eng. B*, 2007, **139**, 1-23.
- [87] C. X. Kronawitter, L. Vayssieres, S. Shen, L. Guo, D. A. Wheeler, J. Z. Zhang, B. R. Antoun and S. S. Mao, *Energy Environ. Sci.*, 2011, **4**, 3889-3899.
- [88] I. Cesar, A. Kay, J. A. Gonzalez Martinez and M. Grätzel, *J. Am. Chem. Soc.*, 2006, **128**, 4582-4583.
- [89] D. L. Smith, *Thin-Film Deposition: Principles and Practice* (McGraw-Hill, Boston), 1995.
- [90] N. Beermann, L. Vayssieres, S.-E. Lindquist and A. Hagfeldt, *J. Electrochem. Soc.*, 2000, **147**, 2456-2461.
- [91] C. D. Chandler, C. Roger and M. J. Hampden-Smith, *Chem. Rev.*, 1993, **93**, 1205-1241.
- [92] R. W. Schwartz, *Chem. Mater.*, 1997, **9**, 2325-2340.
- [93] G. Westin, M. Leideborg, K. Lashgari, V. A. Coleman, K. Jansson and A. Pohl, *Int. J. Nanotechnol.*, 2009, **6**, 828-849.
- [94] R. Knut, J. M. Wickberg, K. Lashgari, V. A. Coleman, G. Westin, P. Svedlindh and O. Karis, *Phys. Rev. B*, 2010, **82**, 094438.
- [95] A. Pohl, G. Westin and K. Jansson, *Chem. Mater.*, 2002, **14**, 1981-1988.
- [96] L. Vayssieres, N. Beermann, S.-E. Lindquist and A. Hagfeldt, *Chem. Mater.*, 2001, **13**, 233-235.
- [97] J. P. Crocombette, M. Pollak, F. Jollet, N. Thromat and M. Gautier-Soyer, *Phys. Rev. B*, 1995, **52**, 3143-3150.
- [98] C. X. Kronawitter, I. Zegkinoglou, C. Rogero, J.-H. Guo, S. S. Mao, F. J. Himpsel and L. Vayssieres, *J. Phys. Chem. C*, 2012, **116**, 22780-22785.
- [99] D. H. Kim, H. J. Lee, G. Kim, Y. S. Koo, J. H. Jung, H. J. Shin, J.-Y. Kim and J.-S. Kang, *Phys. Rev. B*, 2009, **79**, 033402.
- [100] S. Saremi-Yarahmadi, K. G. U. Wijayantha, A. A. Tahir and B. Vaidhyanathan, *J. Phys. Chem. C*, 2009, **113**, 4768-4778.
- [101] F. J. Berry, C. Greaves, J. G. McManus, M. Mortimer and G. Oates, *J. Solid State Chem.*, 1997, **130**, 272-276.
- [102] S. O. Kucheyev, T. van Buuren, T. F. Baumann, J. H. Satcher Jr., T. M. Willey, R. W. Meulenberg, T. E. Felter, J. F. Poco, S. A. Gammon and L. J. Terminello, *Phys. Rev. B*, 2004, **69**, 245102.
- [103] P. Krüger, *Phys. Rev. B*, 2010, **81**, 125121.
- [104] C. X. Kronawitter, M. Kapilashrami, J. R. Bakke, S. F. Bent, C.-H. Chuang, W.-F. Pong, J.-H. Guo, L. Vayssieres and S. S. Mao, *Phys. Rev. B*, 2012, **85**, 125109.
- [105] K. Sivula, *J. Phys. Chem. Lett.*, 2013, **4**, 1624-1633.
- [106] M. V. Nikolic, D. L. Sekulic, N. Nikolic, M. P. Slankamenac, O. S. Aleksic, H. Danninger, E. Halwax, V. B. Pavlovic and P. M. Nikolic, *Sci. Sintering*, 2013, **45**, 281-292.
- [107] N. A. Curry, G. B. Johnston, P. J. Besser and A. H. Morrish, *Phil. Mag.*, 1965, **12**, 221-228.
- [108] P. Kuiper, B. G. Searle, P. Rudolf, L. H. Tjeng and C. T. Chen, *Phys. Rev. Lett.*, 1993, **70**, 1549-1552.
- [109] J. Engel, S. R. Bishop, L. Vayssieres and H. L. Tuller, *Adv. Funct. Mater.*, 2014. doi: 10.1002/adfm.201400203.
- [110] J. Engel and H. L. Tuller, *Phys. Chem. Chem. Phys.*, 2014, **16**, 11374-11380.
- [111] J. E. Katz, X. Zhang, K. Attenkofer, K. W. Chapman, C. Frandsen, P. Zarzycki, K. M. Rosso, R. W. Falcone, G. A. Waychunas and B. Gilbert, *Science*, 2012, **337**, 1200-1203.
- [112] I. A. M. Pohl, L. G. Westin and M. Kritikos, *Chem. Eur. J.*, 2001, **7**, 3438-3445.